

Multi-Annual Flood Mapping using Multi-Sensor Satellite Data in the Iishana Sub-Basin (Namibia/Angola)

Bachelor's Thesis

Julius-Maximilians-Universität Würzburg

Institute of Geography and Geology

Lorenz Beck

Heinestraße 20a, 97070 Würzburg

Bachelor of Science 180 ECTS, PO 2015

Matriculation Number: 2239382

Würzburg, February 2020

1. Supervisor: Dr. Tobias Ullmann
Institute of Geography and Geology, Würzburg
Physical Geography

2. Supervisor: Dr. Sandro Martinis
German Aerospace Center (DLR), Weßling
Department of 'Geo-Risks and Civil Security'
Head of Team 'Natural Hazards'

Acknowledgement

At this point I would like to thank all those, who made it possible for me to work on this bachelor thesis in a unique cooperation between the University of Würzburg, the FU Berlin and the Earth Observation Center of the DLR. Thanks to my official supervisor of the University of Würzburg Dr. Tobias Ullmann for his always ready help during my writing and the establishment of contacts. Thanks also to his working group colleague Robert Arendt of the FU Berlin of the Institute of Geographical Sciences, who provided me with many very valuable data, information and literature about the Iishana Zone in the Cuvelai Basin (Namibia/Angola). Special thanks to the whole team 'Natural Hazards' of the Department of 'Geo-Risks and Civil Security' at the DLR in Oberpfaffenhofen in person of Dr. Sandro Martinis. Many thanks here especially for providing all the used methods and for sharing the data. In this context the TerraSAR-X and the ALOS-2 data were kindly provided by DLR and JAXA (Proposal number MTH1153, PI number 3043), respectively.

Abstract

In this study a remote sensing approach based on multi-sensor satellite data for the creation of different hydrological products is presented. It includes different methods for deriving general water masks from optical multi-spectral remote sensing data and sensors using synthetic aperture radar (SAR), as well as their joint processing. Result layers are calculated for the maximum flood extent, the relative frequencies of flood observations and the total flood duration for all three study years (10/2007 - 09/2008, 10/2008 - 09/2009, 10/2016 – 09/2017). Since the study combines already validated methods, quality layers provide information about the confidence of the results. Further analyses such as the aggregation of the annual results allow insights into the complex surface water dynamics in the transnational study area of the Iishana Zone (Namibia/Angola).

Zusammenfassung

In dieser Studie wird ein fernerkundlicher Ansatz basierend auf multi-sensoraler Satellitendaten zur Erstellung von verschiedenen hydrologischen Produkten präsentiert. Er beinhaltet verschiedene Methoden zur Ableitung von allgemeinen Wassermasken aus optischen multi-spektralen Fernerkundungsdaten und SAR-Sensoren, sowie deren gemeinsame Weiterverarbeitung. Hierbei werden Ergebnisse zum maximalen Flutausmaß, der relativen Häufigkeiten von Flutbeobachtungen und der gesamten Flutdauer für alle drei Untersuchungsjahre (10/2007 - 09/2008, 10/2008 - 09/2009, 10/2016 – 09/2017) einzeln berechnet. Da die Studie bereits validierte Methoden zusammenführt, geben Qualitätslayer Informationen über die Güte der Ergebnisse. Weiterführende Auswertungen, wie die Aggregation der Jahresergebnisse, geben Aufschluss über die komplexen Oberflächenwasserdynamiken im transnationalen Untersuchungsgebiet der Iishana Zone (Namibia/Angola).

Contents

Acknowledgement.....	II
Abstract	III
Zusammenfassung	III
Contents	IV
Figures	VI
Tables	VII
Abbreviations	VII
1 Introduction	8
2 Study Area	10
2.1 Climate	12
2.2 Geomorphology and Hydrology	13
2.3 Soils and Vegetation	15
2.4 Human Geography	16
2.5 Water and Land Use	17
3 Data and Methods	19
3.1 Multi-Sensor Data	19
3.2 Generation of Water Masks	25
3.3 Reprocessing of Water Masks	30
3.4 Product Processing	33
4 Results	35

4.1 Maximum Water Extent (MWE)	36
4.2 Relative Frequency (relFreq)	38
4.3 Total Duration (TD)	40
4.4 Validation	43
5 Discussion	45
5.1 Multi-Sensor Satellite Data for Derivation of Surface Water Products	46
5.2 Surface Water Dynamics of the Iishana Zone.....	51
6 Conclusion and Outlook.....	54
References.....	57
Declaration of Autonomy.....	65

Figures

Figure 1: Overview map of the study area	11
Figure 2: Overflights per sensor and investigation year	21
Figure 3: Temporal resolution and coverage of study area for 10/2007 - 09/2008.....	22
Figure 4: Temporal resolution and coverage of study area for 10/2008 - 09/2009.....	23
Figure 5: Temporal resolution and coverage of study area for 10/2016 - 09/2017	24
Figure 6: Percentage of annual spatial coverage of the study area per sensor and investigation year	25
Figure 7: Flowchart of processing	27
Figure 8: Visualization of the Binary Mask Processor.....	32
Figure 9: ‘Maximum Water Extent’ for each year (A, B, C) and their mean and relative range (D), as well as corresponding zooms.....	37
Figure 10: ‘Relative Frequency’ for each year (A, B, C) and their overall and relative range (D), as well as corresponding zooms.....	39
Figure 11: ‘Total Duration’ for each year (A, B, C) and their mean and relative range (D), as well as corresponding zooms.....	41
Figure 12: Comparison between the ‘Frequency Distribution’ of 'Total Duration' of the three investigation periods.....	42
Figure 13: Two ‘Quality Layers’ for each year, including the 'Number of uncertain Days' and the Ratio ‘FloodObservations(FO) * 100 / TD’	44
Figure 14: Number of valid observations per investigation year.	50
Figure 15: Connected drainage systems in dependence on the years of water occurrence.....	52

Tables

Table 1: Overview of all used SAR products20

Table 2: Overview of all used multi-spectral products.....20

Abbreviations

AOI	Area of Interest
ALOS	Advanced Land Observing Satellite
AMSR-E	Advanced Microwave Scanning Radiometer – Earth Observation
CB	Cuvelai Basin
DLR	German Aerospace Center
ESA	European Space Agency
FO	Flood Observations
ICSMD	International Charter Space and Major Disaster
IWRM	Integrated Water Resource Management
MODIS	Moderate-Resolution Imaging Spectroradiometer
MWE	Maximum Water Extent
NUD	Number of uncertain Days
QL	Quality Layers
RaMaFlood	RapidMappingFlood
relFreq	Relative Frequency
SAR	Synthetic Aperture Radar
TD	Total Duration
WO	Water Occurrence
ZKI	Center for Satellite Based Crisis Information

1 Introduction

The number of natural hazards is increasing worldwide (Skakun et al. 2014). Climate change plays a major role here, above all through an intensification and rise of extreme hydrological events (Farmer 2015; Gilau et al. 2011; Thomson 2018). With 40% of all, floods are the most common geo-risks (Persendt et al. 2015), affecting about 1 billion people which currently live in flood-prone regions and this number could possibly double by 2050 (Long et al. 2014). Simultaneously these intensified hydrological cycles also result in droughts, which among natural hazards on average cost the most lives (Persendt et al. 2015; Thomson 2018). Climatically highly variable semi-arid regions with seasonally inundated floodplains have to face both hazards: Flooding and droughts (Gilau et al. 2011). Here particular importance lies in understanding the spatiotemporal pattern of surface water dynamics. Further factors like large-scale land use and land cover change, as well as increasing water demand by agriculture, industry and domestic use reinforce this relevance (Angula and Kaundjua 2016; Kluge et al. 2008; Marsh 1992; Mendelsohn et al. 2013; Tulbure et al. 2016).

The study area, the Iishana Zone in the Cuvelai Basin (CB), a rapidly developing rural area in northern Namibia and southern Angola, represents one such affected region (Calunga et al. 2015; Mendelsohn et al. 2013; Persendt et al. 2015). Due to highly variable rainfall over time and space, it can be confronted with severe floods and droughts, causing crop failures and restrictions in food security (Mizuochi et al. 2014). A further complicating factor here is data scarcity. Missing gauge measurements, a lack of long-time data series and not well-defined drainage lines make it difficult to understand the large and complex hydrological system with its wide varying channels and pans (Awadallah and Tabet 2015; Goormans et al. 2015; Mendelsohn et al. 2013; Mendelsohn and Weber 2011; Mufeti et al. 2013; Persendt and Gomez 2016; Persendt et al. 2015). Here earth observation by remote sensing with its increasing data volumes and availability can make a major contribution for flood risk assessment providing

valuable high spatial and high temporal information (Awadallah and Tabet 2015; Martinis et al. 2015a; Wieland and Martinis 2019).

Existing work was already carried out on the study area using remote sensing methods. Studies have been conducted using weather satellites to evaluate past and present levels of meteorological rainfall events to understand climatic patterns (Awadallah and Tabet 2015; Mendelsohn and Weber 2011; Persendt et al. 2015). Paired with digital terrain models, these data are also used for hydrological modelling (Goormans et al. 2015; Mufeti et al. 2013) and partly extraction of the drainage network of the study area (Persendt and Gomez 2016). Furthermore data from the passive sensor Advanced Microwave Scanning Radiometer – Earth Observation (AMSR-E) and its follower mission AMSR-E 2 were also used to gain an understanding of surface flooding (Groeve 2010) and to assess new agricultural potentials such as rice cultivation in synthesis with scenes from the Moderate-Resolution Imaging Spectroradiometer (MODIS) (Hiyama et al. 2014; Mizuochi et al. 2014). However, up to now the focus has usually been either on a spatially coarse resolution survey of the entire Iishana Zone or more precise analyses carried out in a smaller area of interest (AOI). In terms of methodology, the work should therefore be oriented towards sensor-multiple studies, which take aggregations of flooding observations into account with higher resolution in time and space. The comparison of different seasonal or annual flood extents derived from multi-spectral Landsat data (Skakun et al. 2014; Tulbure et al. 2016) together with radar data (Long et al. 2014) as well as their further processing, for example to frequency maps (Skakun et al. 2014) are of special interest.

Therefore, this thesis focuses on the synthesis of different flood or water masks. These two terms (flood and water) are used synonymously due to the high variability of the occurrence of surface water and the almost missing existence of permanent water. To derive these flood or water masks, multi-sensor satellite data (Töyrä et al. 2001) from sensors using synthetic aperture radar

(SAR) like Envisat-ASAR, Advanced Land Observing Satellite (ALOS)-PALSAR, its successor ALOS2-PALSAR, TerraSAR-X and Sentinel-1 as well as the optical satellites Landsat 5 and Landsat 8 are used and methods developed by the German Aerospace Center (DLR) are applied (Martinis et al. 2015a; Martinis et al. 2015b; Twele et al. 2016; Wieland and Martinis 2019). The goal is to generate, compare and aggregate annual hydrological products with high spatial and temporal information density (Shakya 2018), which contributes to the understanding of the runoff system in the Iishana Zone and thus can be used in the context of sustainable water and land use as well as for flood risk management.

2 Study Area

This work focuses on the central western part of the Cuvelai Basin (CB) (figure 1, p.11). The CB is surrounded by the Cunene River Basin in the west and the Okavango River Basin in the east and includes nine major hydrological drainage zones (Faulstich et al. 2018; Mendelsohn et al. 2013). One of these is the Iishana Zone, which represents the study area of this thesis. With a size of about approximately 18,000 km² the study area encloses the Omadhiya Lakes in the southeast, borders the Cunene River (both figure 1, p.11) in the northwest and is located with a little more than half in Namibia and the rest in Angola, which are separated by the border at 17° 23' S (Faulstich et al. 2018). Due to this transboundary location, the Iishana Zone has no clear administrative boundaries, but is rather a natural area. Following Faulstich et al. 2018, it extends diamond-shaped meridionally from 16° 28' S to 18° 14' S and zonally from 14° 30' E to 16° 00' E (figure 1, p.11). This overlaps largely with the Iishanas outline defined by Mendelsohn et al. 2013. Subsequent processing of raster data will only take the extent and not the shape of the study area into account and therefore the results will include parts of the Cunene River and most of the Central Drainage to the east (Mendelsohn et al. 2013). This chapter is to focus on

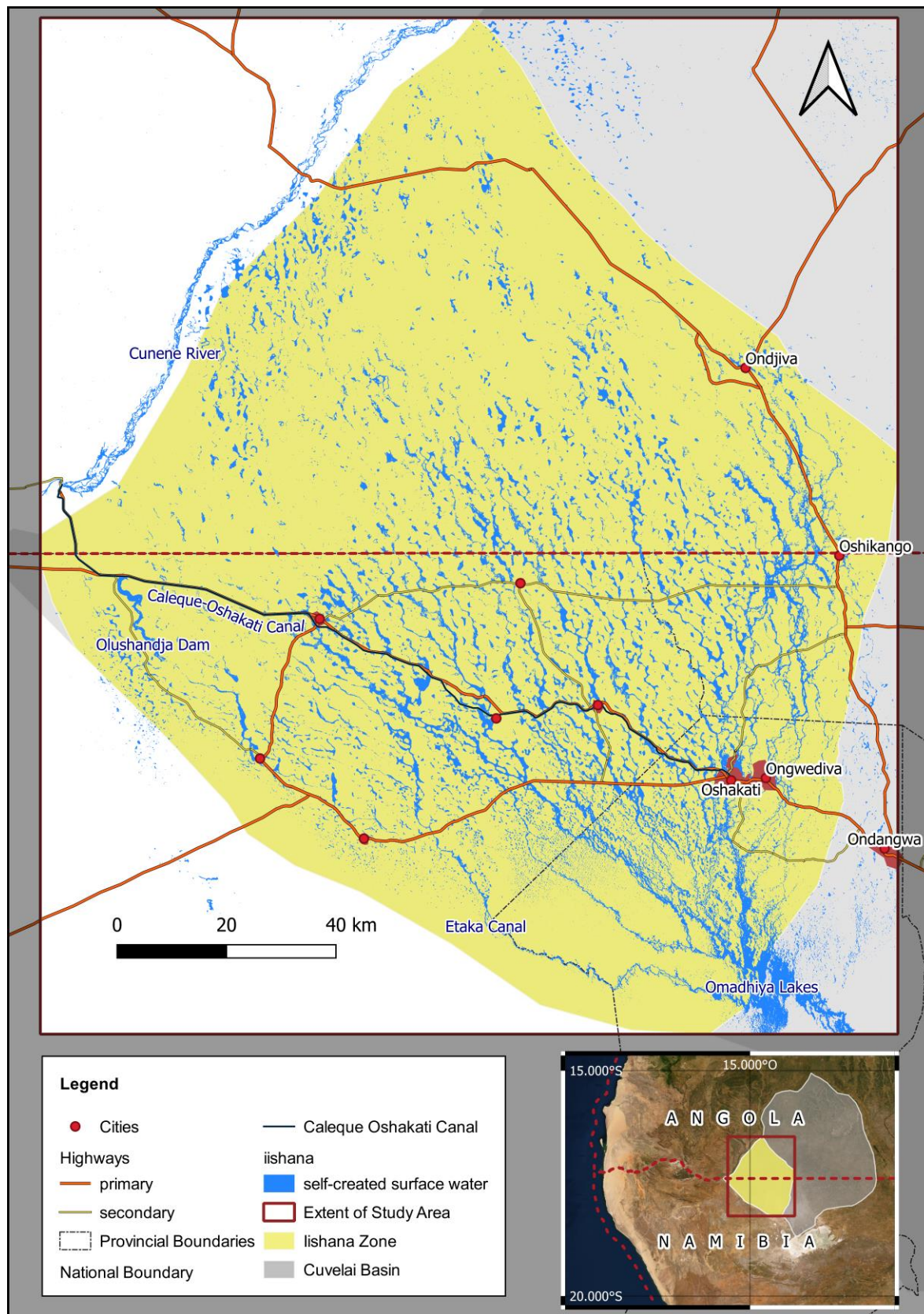


Figure 1: Overview map of the study area

the natural and anthropogenic characteristics of the Iishana Zone, which are relevant in the context of this study. This includes the climate, geomorphology and hydrology, soils and vegetation as well as selected aspects of human geography, like infrastructure or settlements together with their population and their water and land use.

2.1 Climate

The semi-arid climate in the Iishana Zone is subject to the seasonally changing influences between subtropical high-pressure systems (in dry season / winter) and the inter-tropical convergence zone (in rainy season / summer). During the warmer rainy season from October (Mendelsohn et al. 2013) / November (Faulstich et al. 2018; Persendt et al. 2015) to April the humid air masses from the equator bring more than 99% of the annual precipitation (Marsh 1992), especially in January, February and March. In the colder winter months from May to September (Mendelsohn et al. 2013) / October (Faulstich et al. 2018; Persendt et al. 2015) the sinking air masses of the anticyclones cause clouds to dissipate and thus are the reason for the dry season (Faulstich et al. 2018; Mendelsohn et al. 2013; Persendt et al. 2015). According to the effective climate classification of Köppen and Geiger, the Iishana Zone is assigned to a hot-arid steppe climate (BS_h) (Kottek et al. 2006). This is confirmed by high average annual temperatures of 22°C (Mendelsohn et al. 2013) to 24° C (Kaseke et al. 2016) with monthly peak-means of 35° C to 40° C during the earliest summer months (Mendelsohn et al. 2013). Additionally the ratio between the mean annual precipitation from 350 mm – 550 mm (Faulstich et al. 2018; Mendelsohn et al. 2013) / 700 mm (Kaseke et al. 2016) and the potential evapotranspiration from 2200 mm (Kaseke et al. 2016) / 2600 mm – 3200 mm (Faulstich et al. 2018; Mendelsohn et al. 2013) shows the aridity of the Iishana Zone (Kaseke et al. 2016; Mendelsohn et al. 2013).

However, these fuzzy values show a general spatial distribution over the CB with its Iishana Zone. While the mean annual precipitation increases from southwest to northeast of the Iishana

Zone, the mean annual potential evapotranspiration rises in opposite direction from northeast to southwest (Mendelsohn et al. 2013). But even more important for understanding the climate is its high inter- and intra-annual variability. While not only annual precipitation sums vary strongly between 25% in the northeast to 40% in the south, their temporal onset and duration during the rainy season is also different. An additional missing pattern of the recurrence of precipitation over decades makes it increasingly difficult to use the land and its water (Calunga et al. 2015; Faulstich et al. 2018; Marsh 1992; Mendelsohn et al. 2013; Persendt et al. 2015). This is also marked by the convective heavy rainfalls in the later months of summer, which usually come down in less than an hour with afternoon thunderstorms. These showers are locally concentrated and variable in their spatial occurrence (Mendelsohn et al. 2013).

2.2 Geomorphology and Hydrology

With an altitude of 1100m to 1200m above sea level, the geomorphological large-scale terrain of the Iishana Zone falls with an extreme low slope gradient of 1 ‰ in Angola and 0.5 ‰ in Namibia from northwest towards to southeast (Faulstich et al. 2018; Mendelsohn et al. 2013). The characteristic landscape of the Iishana Zone as one of the major six landscapes in the CB has been formed by older and recent aeolian and fluvial processes. This resulted in a flat, extensive network of not-well defined channels, interconnected or isolated water pans (in Namibia: singular: *oshana*, plural: *iishana*) and ridges (*omitunda*) in between, with even slight differences in topography of less than 10m (Mendelsohn et al. 2013; Persendt and Gomez 2016).

Rainfall fills these small geomorphological depressions and channels with water, creating partly episodic and partly ephemeral water bodies (Awadallah and Tabet 2015; Faulstich et al. 2018). This accumulation of water is then used by humans, animals or plants. In some cases it evaporates, infiltrates, stands or even flows over the flat web of channel southwards, depending on the amount of precipitation (Marsh 1992; Mendelsohn et al. 2013). Drainage through the very wide channels, which are generally narrower in the east and wider in the west (100m to

2km), occurs erratically and can be stopped by re-routing meandering or inland deltas (Faulstich et al. 2018; Mendelsohn et al. 2013; Persendt and Gomez 2016). Only with larger sums of precipitation the *iishana* (figure 1, p.11) can interconnect and flow south into the Omadhyia Lakes, which in turn can drain the water masses endorheically via the Ekuma River into the Etosha Pan (Awadallah and Tabet 2015; Goormans et al. 2015; Marsh 1992; Mendelsohn et al. 2013; Persendt et al. 2015; Strohbach 2008).

It is therefore assumed that during more extreme rainfall water from southern Angola will combine with those in Namibia and cascade into further *iishana*. According to Faulstich et al. 2017, the last two decades have seen especially high precipitation in 2008, 2009, 2010, 2011, 2013 and 2017. Particularly high floods (*efundja*) have occurred 11 times over the last 73 years (status 2013 and including 13 years of no information), such as in 2008, 2009 and 2011 (Awadallah and Tabet 2015; ICSMD 2009; Mendelsohn et al. 2013; Persendt et al. 2015; ZKI 2008, 2009). With water depths of up to 7m these floods reach levels that endanger human lives, their health, cause damage to property, infrastructure and economic losses in agriculture, industry, commerce and tourism (Faulstich et al. 2018; Mandl et al. 2012; Mendelsohn et al. 2013; Ministry of Agriculture, Water and Forestry of Republic of Namibia 2011; Persendt et al. 2015; Shifidi 2016). For instance in 2009, 102 people died by the impacts of flooding and 65,000 were displaced from their homes (Mendelsohn et al. 2013). Although this pluvial flooding occurs variably from year to year due to the dependence of precipitation and following no recurrence-pattern (Awadallah and Tabet 2015; Faulstich et al. 2018), an increase in the extent and severity of the floods can be observed compared to previous decades. This is due to soil erosion on the *omitunda* which accumulates in the *iishana*, raising them and thus causing larger areas of flooding due to decreasing differences in relief (Mendelsohn et al. 2013; Persendt et al. 2015). This development highlights the need for future disaster risk reduction, including early warning systems, vulnerability analyses and a basic understanding of the hydrology of the *iishana*

(Amadhila et al. 2013; Awadallah and Tabet 2015; Calunga et al. 2015; Faulstich et al. 2018; Filali-Meknassi et al. 2014; Gilau et al. 2011; Mendelsohn et al. 2013). This also involves a post-event risk assessment to determine the severity of the flooding by means of maximum spatial dimensions, its duration and the average magnitude within the year (Awadallah and Tabet 2015).

This will be of particular importance when analyzing the advantages of moderate floods, which occurred approximately 30 times in the last 73 year (status of 2013 and including 13 years of no data) (Persendt et al. 2015). These are necessary for any land use in the Iishana Zone and refilling groundwater aquifers by infiltration through sand (Marsh 1992; Mendelsohn et al. 2013; Niipele et al. 2015). Thus underlying calcrete and limestone layers can form a multi-strata aquifer system at a depth of 10m - 80m. Due to the permeability of the sandy sediments, the groundwater has a fundamental salinity and can be polluted by fluorides, nitrates and sulphates (Christelis and Struckmeier 2001; Faulstich et al. 2018; Mendelsohn et al. 2013; Persendt et al. 2015). Especially in dry years, when the availability of surface water of the *iishana* is very low to non-existing, the partly easy access to shallow groundwater plays a major role. Droughts like recently in three consecutive years from 2013 to 2015, where particularly little precipitation fell, can lead to a strong restriction of food security and thus to fatalities and economic losses (Faulstich et al. 2018; Kerdiles et al. 2015; Lütke-meier and Liehr 2015; Calunga et al. 2015)..

2.3 Soils and Vegetation

The soils of the Iishana Zone are influenced by geomorphological and climatic conditions and thus represent different degrees of influence by water, wind and evapotranspiration. While the east is generally sandier and the south more saline, the small-scale differences in relief usually determine the composition of wind-blown sands on the *omitunda* and alluvial clays on the ground of the *iishana*. Especially the transition zones between the low-lying channels and the higher ridges are among the most fertile soils of the region and can be assigned to cambisols

and calcisols, while in the south saline arenosols can additionally occur. At the same time, dissolution and precipitation processes can lead to the formation of near-surface crusts of silicate, lime or clay, which forms impermeable layers and thus reduce infiltration and increase surface runoff (Faulstich et al. 2018; Mendelsohn et al. 2013; Persendt and Gomez 2016).

All conditions described so far are also reflected in the spatial and temporal distribution of the vegetation. Differences across the Iishana Zone can be especially seen along the higher *omitunda*, where a woody vegetation mix of shrub and tree savannah is found together with the dominant species *Colophospermum mopane*. On these ridges, mopane shrubland with growth heights of 1m - 3m can be found in the southwest, while mopane woodland with somewhat larger vegetation can be found in the north. These are supplemented in the east by Kalahari woodlands, which grow patchy on the larger sandy areas, and by Makalani palms on somewhat more saline soils (Faulstich et al. 2018; Leggett et al. 2003; Mendelsohn et al. 2013; Strohbach 2001; Wagenseil and Samimi 2007). In contrast, the more frequently flooded *iishana* are mostly covered by grasslands, due to saline and loamier conditions. Especially in the south saline grasslands prevail with up to 150 different species (Marsh 1992; Mendelsohn et al. 2013).

In addition to this spatial variability, the seasonal nature of the rainy and dry periods also plays a major role in the occurrence of vegetation. Especially the growth of the grasses is dependent on the availability of surface water and therefore shows a high seasonal and inter-annual variability. (Hassler et al. 2010; Leggett et al. 2003; Mayr and Samimi 2015; Mendelsohn et al. 2013; Wagenseil and Samimi 2007).

2.4 Human Geography

Due to the fertility of the soils and the availability of surface water, the CB is the most densely populated rural region in Namibia (with almost 40% of the population of the country) and also one of the most populous in all of southwestern Africa. In 2013, approximately 1.3 million

people lived in the CB, 70% of them in Namibia and 30% in Angola (Mendelsohn et al. 2013). Within this basin, the Ishana Zone has the highest population density with up to 40 (Mendelsohn et al. 2013) - 100 (Persendt et al. 2015) people per square kilometer. Only about 20% of the population lives in cities, the majority in one metropolitan area on the Namibian side, including Oshakati (2011: 36,541) and its twin city Ongwediva (2011: 20,260), which together is a fast growing administrative and commercial area (figure 1, p.11). Other towns as Ondangwa (2011: 22,822) and Oshikango in Namibia or the comparatively small provincial capital Ondjiva in Angola are dominated by transnational trading (figure 1, p.11). They are connected by a major trunk road, which plays an important economic role with a daily exchange of millions of US dollars (Awadallah and Tabet 2015; Mendelsohn et al. 2013; Muir and Hattingh 2012).

2.5 Water and Land Use

The fact that this populated natural area is only separated by an administrative transnational border is proven not only by the common origin of the people from the Owambo tribe, but also by the similarities of their ways of living, represented by their land and water use (Mendelsohn et al. 2013).

The water supply of the Ishana Zone is generally tripartite. First, the surface water of the Ishana Zone represents the most important source for most of the population, although it is heavily polluted, making it harmful to health and not suitable for drinking. Secondly, different types of groundwater are used. Because the easy-accessible surface-near groundwater can be heavily polluted, at some places deeper groundwater layers are occasionally drilled into, in order to use its water for consumption. In addition, the Calque-Oshakati Canal (figure 1, p.11) was built in 1973, which carries water from the Cunene River to Oshakati and is used as the main source for drinking water by the population at four official tapping points. Illegal use, however, also

reduces and pollutes the open water masses provided by the canal (Faulstich et al. 2018; Kluge et al. 2008; Mendelsohn et al. 2013).

Naturally and originally an agro-silvi-pastoral system is predominant, a combination of rain-fed subsistence agriculture (especially pearl-millet, supplemented by sorghum, corn and peanut), pastoral livestock farming (especially cattle, goats and donkeys) and small-scale deforestation as fuel and building material (Hooli 2016; Kerdiles et al. 2015; Marsh 1992; Mendelsohn et al. 2013; Newsham and Thomas 2011). Even today almost exclusively rain-fed agriculture with pearl millet (*mahangu*) is practiced as well as extensive livestock farming, but in general hardly produced for sale. Rather a generally high variety of livelihoods is caused by the rapid social transition from subsistence to cash economy. Pastoralism and agriculture is thus often practiced alongside another main employment (Faulstich et al. 2018; Hiyama et al. 2014; Mendelsohn et al. 2013; Newsham and Thomas 2011; Niipele et al. 2015). Simultaneously local specialization of land use is also evident as irrigation systems are built in places along the Etaka Canal south of the Olushandja Dam (figure 1, p.11) and most of the cattle are concentrated on a few owners. Due to this departure from indigenous land use systems and the increasing population, there is a general pressure to the use of the resources of land and water (Niipele et al. 2015). Therefore, land degradation is clearly visible, in particular from space by the differences along the national border. While on the Namibian side the land appears brownish due to a higher population density and higher pressure of land and water use, the less populated area of Angola appears much greener (Marsh 1992; Mendelsohn et al. 2013).

3 Data and Methods

The aim of this chapter is to describe the different input data in the context of the multi-sensor approach and to explain their step-by-step processing. In the methods section, general principles of water detection by remote sensing and the resulting different generation processes of water masks are described as well as their further processing and the methods of the final hydrological products.

3.1 Multi-Sensor Data

Due to the generally low availability of data for the analysis of hydrological phenomena in the Ilishana Zone, an application of remote sensing data in this area shows great potential (Awadallah and Tabet 2015; Persendt et al. 2015; Persendt and Gomez 2016). Since one goal of the study is a final product of temporal dimension with the unit of days, it is important to achieve the best possible temporal resolution over the periods of investigation. Especially since not only one hydrological flood event of a few weeks is analysed, but the dynamics of surface water over a whole year. In addition, no sensor-specific products are generated or required, since the calculation of the flooding duration is based on general water masks (Shakya 2018). This offers a remote sensing multi-sensor approach (Martinis et al. 2015b; Wieland and Martinis 2019), whereby firstly the temporal repetition rate of observations can be significantly improved, and at the same time the advantages and disadvantages of different sensors for water detection can be balanced, but also mutually reinforced (Long et al. 2014; Töyrä et al. 2001). A detailed data research, taking in account several possible investigation periods, data accessibility, sensor-specific appropriateness of products and already existing processing chains, resulted in the use of multi-spectral optical data as well as SAR data. Table 1 and 2 (p.20) provide an overview of the sensors included in the analysis. Wet and dry season are combined to form an annual basis (October – September of following year) for the investigation periods. 10/2007 – 09/2008 and 10/2008 – 09/2009 are selected due to markable flood events (Amadhila et al. 2013; ICSMD

2009; Mendelsohn et al. 2013; Persendt and Gomez 2016; Persendt et al. 2015; ZKI 2008, 2009) and 09/2016 – 10/2017 because of a high precipitation sum (Faulstich et al. 2018) and to incorporate the new available data from the Sentinel-1 mission embedded in the Copernicus Program of the European Space Agency (ESA).

Table 1: Overview of all used SAR products (Airbus Defence and Space 2015; Buckreuss et al. 2008; ESA 2019a, 2019b; Miranda 2016)

Product Name	Final Pixel Spacing (m)	Coverage (km: Range*Azimuth)	Polarizations
ALOS PALSAR – FBS GEC*	6.25	70*90	SinglePol HH
ALOS PALSAR – FBD GEC*	12.5	70*90	DualPol HH+HV
ALOS PALSAR – PLR GEC*	12.5	30*90	QuadPol HH+HV+VH+VV
ALOS2 PALSAR – SM3 FBD 1.1*	10	70*70	DualPol HH+HV
Envisat ASAR – IMP	12.5	70-90*110-130	SinglePol (VV HH)
Envisat ASAR – WSM	75	400-450*variable	SinglePol (VV HH)
Sentinel-1B GRD	10	250*175	DualPol VV+VH
TSX-ScanSAR	7.5	100*150	SinglePol HH
TSX-Stripmap	2.5	15-30*50-75	SinglePol HH
TSX-Spotlight	2	10*10	SinglePol HH

* Product Level: ESA *GEC* = JAXA *1.5*, ESA *SLC* = JAXA *1.1*

Table 2: Overview of all used multi-spectral products (United States Geological Survey 2019)

Product Name	Pixel Spacing (m)	Coverage (km)	Bands	Repetition Time (days)
Landsat 5 L1	30 (bands 1-5, 7)	170*183	7	16
Landsat 8 L1	30 (bands 1-7, 9-11)	170*185	11	16

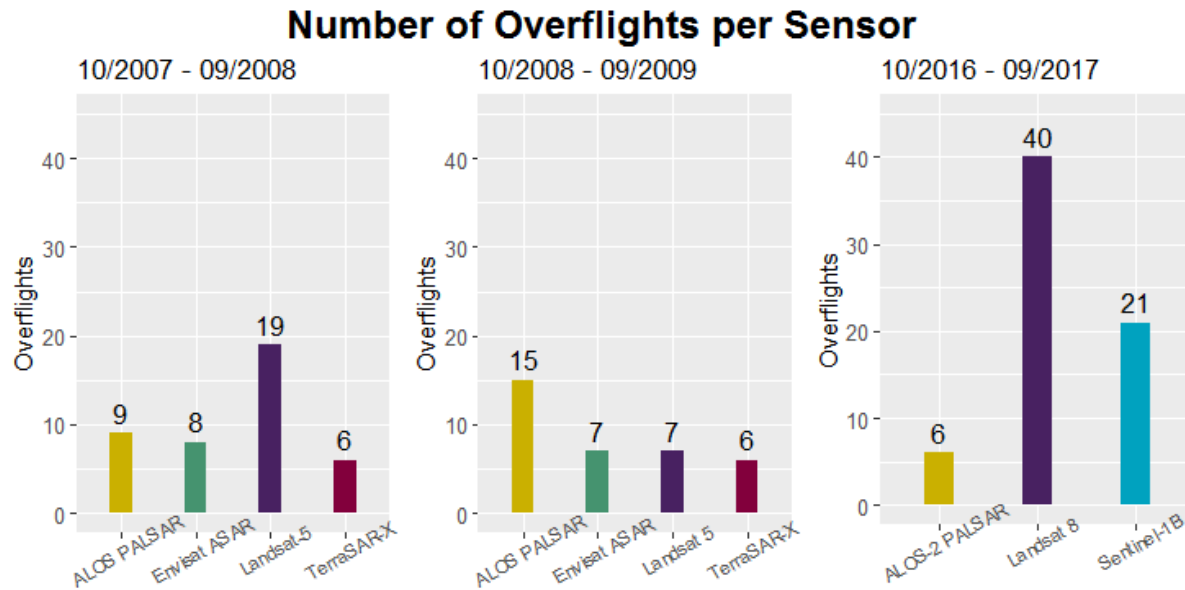


Figure 2: Overflights per sensor and investigation year

Especially in the field of radar data, a larger variety of different sensors and products is used for the investigation of the years 2007/2008 and 2008/2009 (figure 2). This is due to a low repetition rate of observations over time, caused by earlier more event-based and commercial missions like TerraSAR-X (Buckreuss et al. 2008) or ALOS(2) PALSAR (Persendt and Gomez 2016; Rosenqvist et al. 2007) instead of contiguous automated open data sensing like Sentinel-1 (Potin et al. 2016; Twele et al. 2016). An example can also be seen in figure 3, p.22 (2007/2008 mid to end of March) and figure 4, p.23 (2008/2009 early March), where a significantly higher observation frequency occurs during acute flooding periods (ICSMD 2009; ZKI 2008, 2009). These figures also show the strong difference in data density between the first two periods of investigation and the last 2016/2017, which is also evident in the much more systematic distribution of data over time in figure 5 (p.24).

Temporal Resolution and Coverage per Sensor (10/2007 - 09/2008)

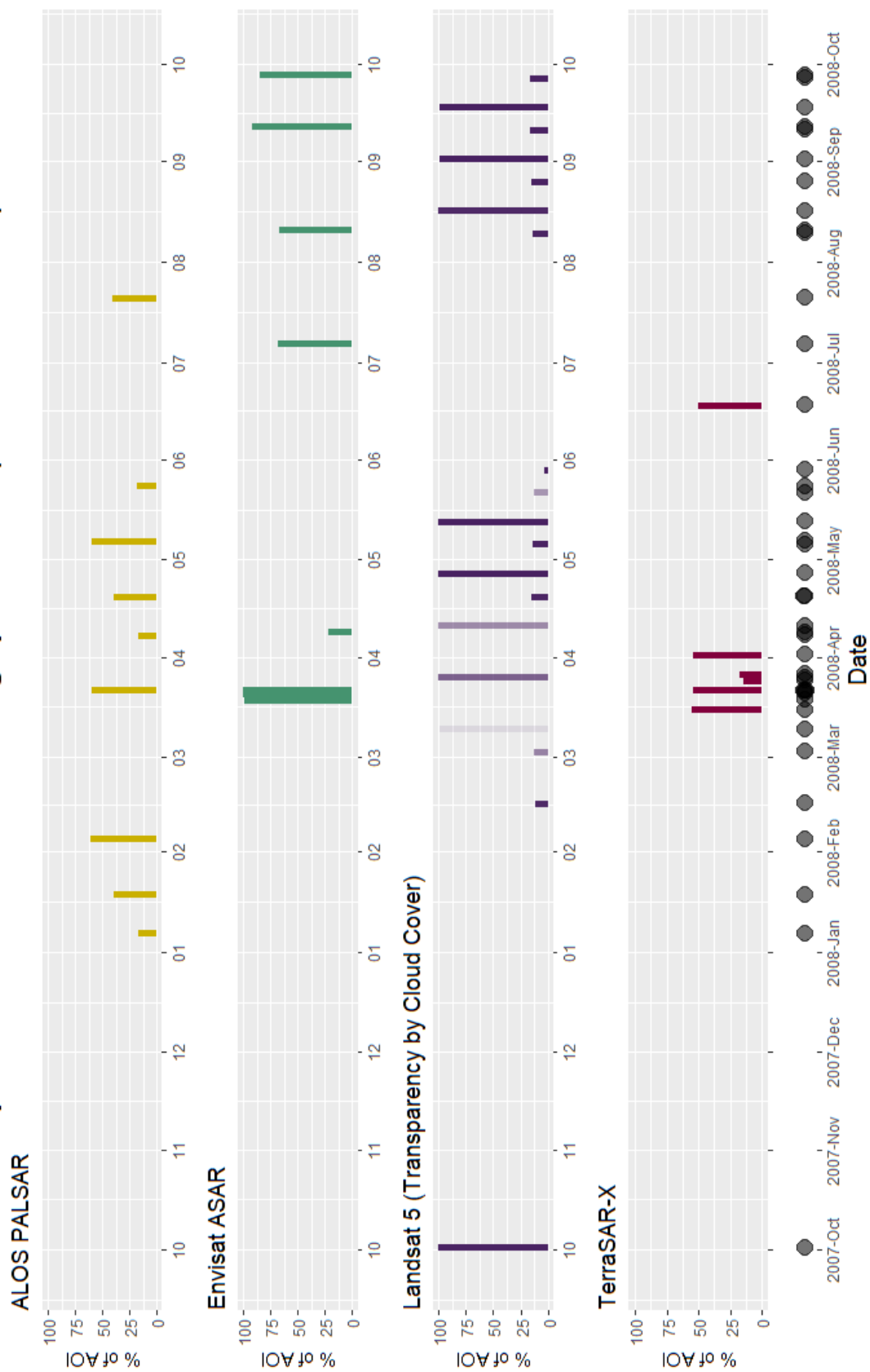


Figure 3: Temporal resolution and coverage of study area for 10/2007 - 09/2008

Temporal Resolution and Coverage per Sensor (10/2008 - 09/2009)

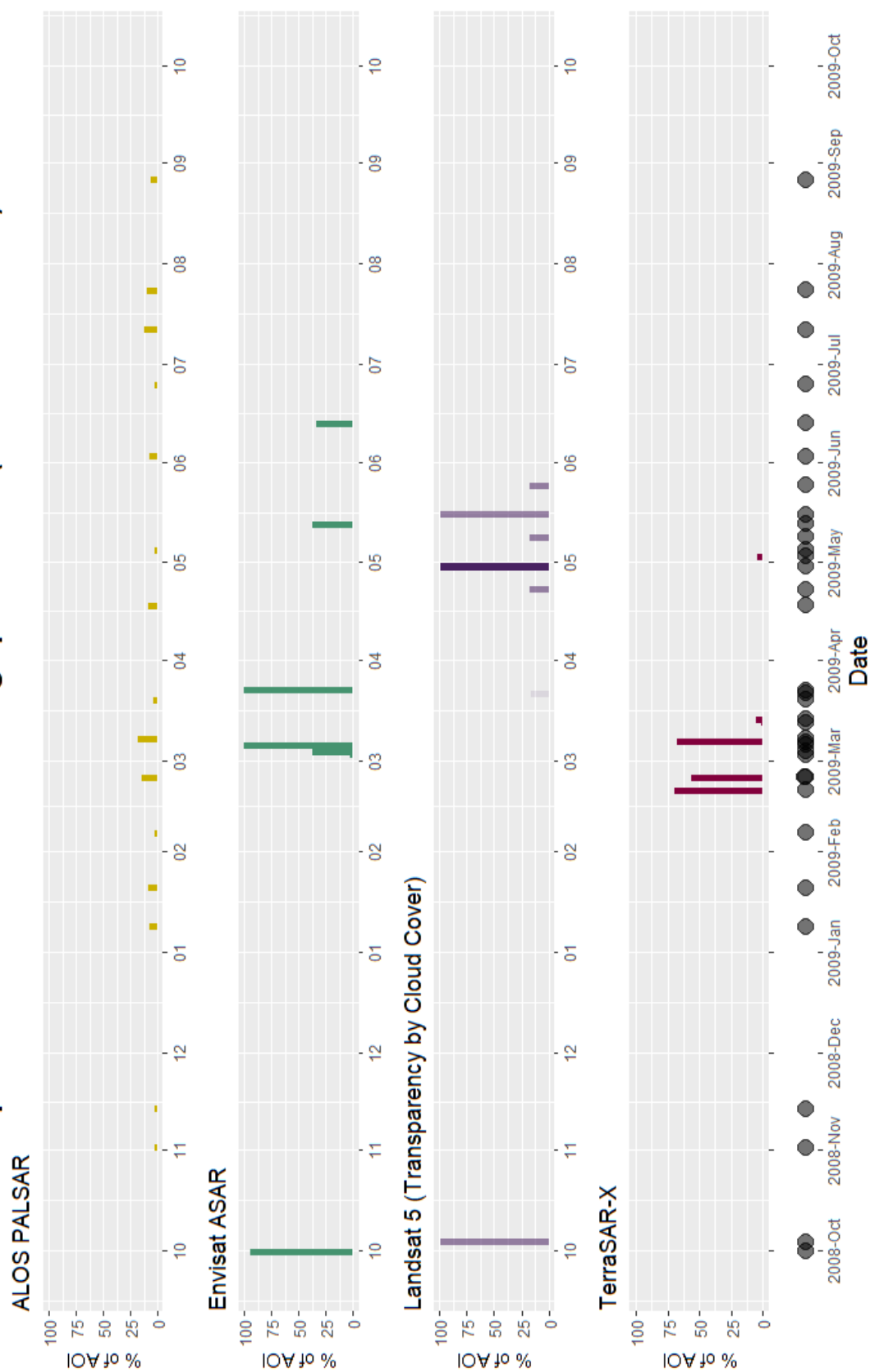


Figure 4: Temporal resolution and coverage of study area for 10/2008 - 09/2009

Temporal Resolution and Coverage per Sensor (10/2016 - 09/2017)

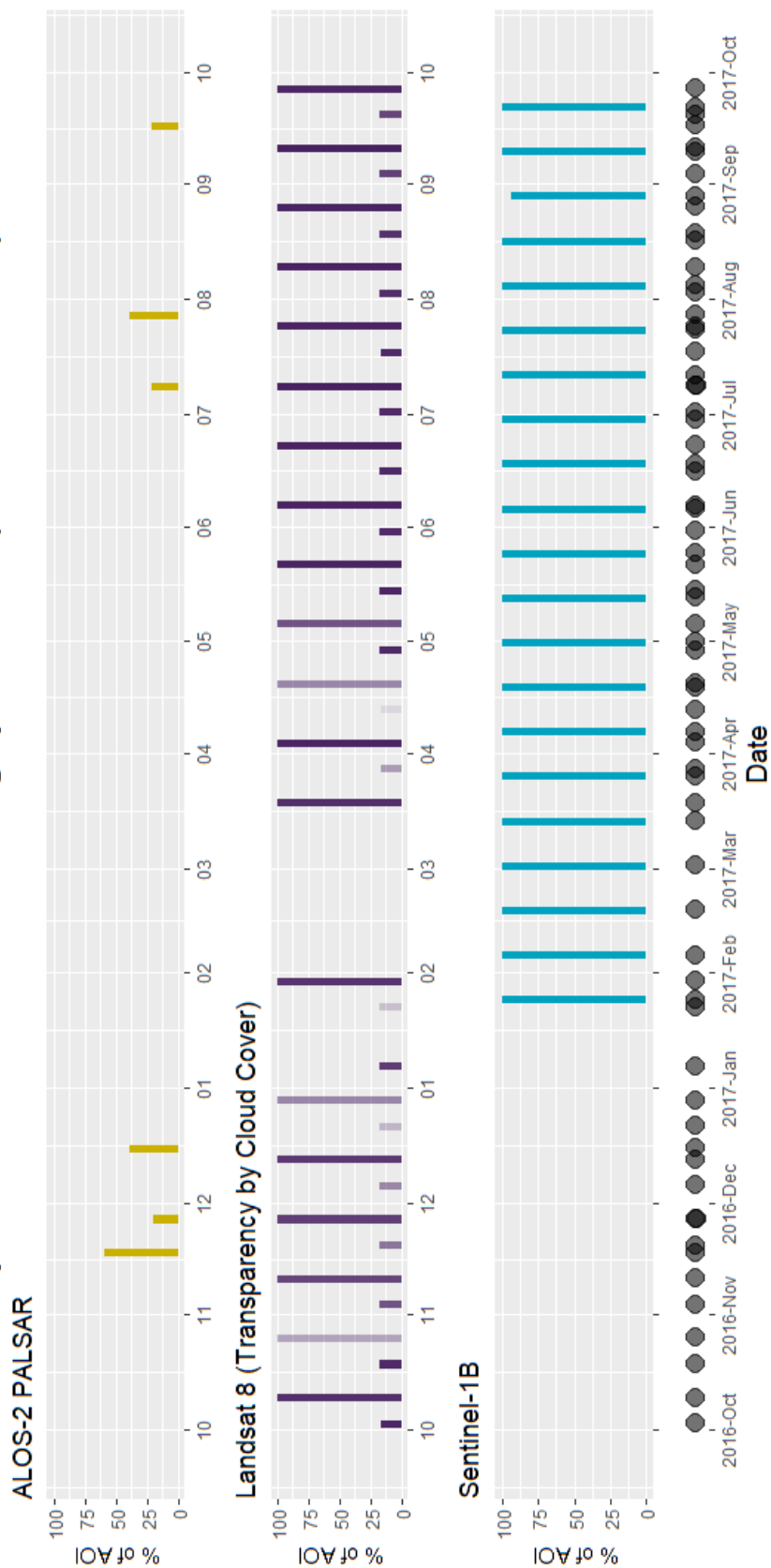


Figure 5: Temporal resolution and coverage of study area for 10/2016 - 09/2017

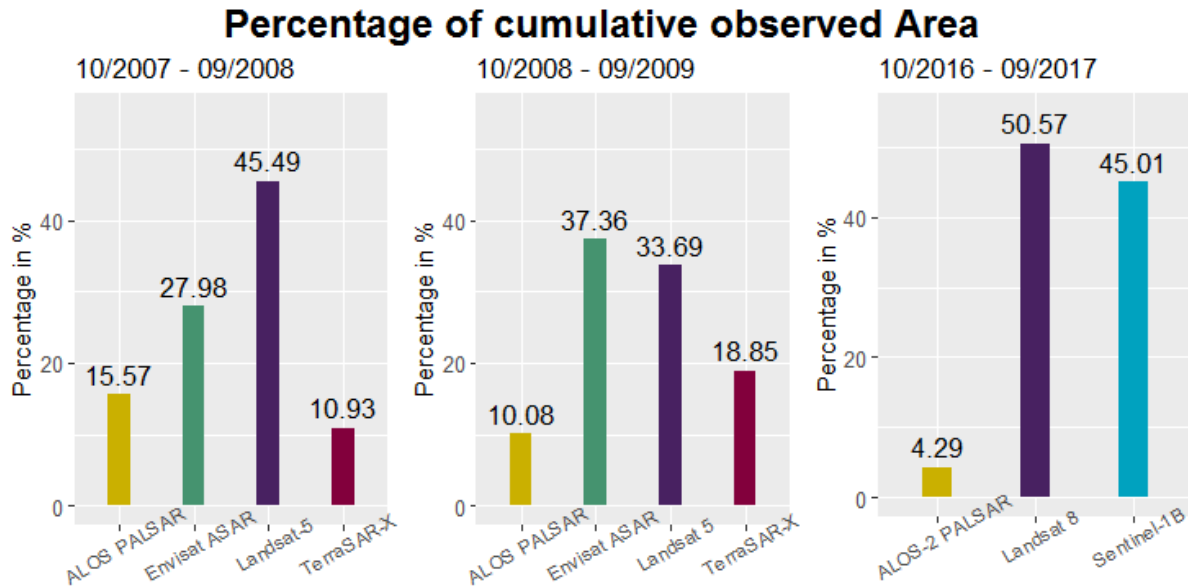


Figure 6: Percentage of annual spatial coverage of the study area per sensor and investigation year

It should also be mentioned that the sensed coverage per overflight of the study area is very different. In addition to the sensor properties like range or azimuth distances (table 1 and 2 p.20), this is also reflected per overflight and sensor in the figures of the temporal resolutions per investigation year (figure 3-5, p.22-24). Figure 6 shows a summary of these years comparing the different sensors in their proportion of the spatial sum of all cumulative overflights. This confirms the enormously improved resolution in 2016/2017, especially by Sentinel-1, as well as high contrasts between the number of overflights per sensor in figure 2 (p.21) and their respective share of the cumulative coverage (figure 6), for example between ALOS PALSAR and Envisat ASAR in 2008/2009.

3.2 Generation of Water Masks

For the derivation of surface water masks different challenges exist for optical and SAR data. It is obvious that the usefulness of optical data is severely limited by clouds, which is an immense disadvantage due to the coupling of floods to precipitation. However, in cloudless views water surfaces can be easily detected by these passive sensors due to the contrasting spectral signature of water, which shows very low reflection values, to other land coverings. Also unfavorable sun-

sensor-surface geometries can lead to sun glint effects, which erroneously can increase the actually low reflection strongly (Jensen 2016; Martinis et al. 2015b; Wieland and Martinis 2019). Active sensor systems, operating with electromagnetic wavelengths in the microwave range, allow radar satellites to avoid exactly these problems and capture scenes both during cloud cover or at night (Jensen 2016; Martinis et al. 2015b). Since smooth water surfaces show very low or no backscattering values in radar data and can therefore stand out strongly from surrounding areas, SAR satellites are considered by scientific consensus to be the most common way of detecting surface water (Long et al. 2014; Martinis et al. 2015b). Water detection is therefore strongly dependent on surface properties and on their interaction with the used wavelength (Jensen 2016; Li and Yang 2015). Thus, it can happen that water is not detected, when the water surface roughness is increased by waves or double-bounce effects caused by vegetation. In turn areas can also be erroneously classified as inundated, when other smooth surface structures such as agricultural areas, sand, bare ground or asphalt are involved. Although it is possible for SAR sensors to distinguish between flooded vegetation and non-flooded vegetation, flooded vegetation areas are not considered in this study. (Martinis et al. 2015b; Martinis et al. 2018; Williams and Greeley 2004). Sensor internal differences also play an important role. While the X-band waves interact much stronger at the direct surface, the middle C-Band and the even longer L-band waves penetrate deeper into the land cover, which leads to a decreasing contrast between water and non-water areas for longer wavelengths (Twele et al. 2016). Furthermore, co-polarized images, receiving the same polarization of the waves as sent (for example HH or VV) are preferable to cross-polarized acquisitions (for example HV), which are mainly volume scattering sensitive. Within the co-polarized scenes, HH polarizations are more suitable than VV, since VV polarizations are more susceptible to vertical structures like waves (Li and Yang 2015; Long et al. 2014; Martinis et al. 2015b; Oliver and Quegan 2004).

In the following, the different methods for surface water detection (figure 7: The three boxes on the left) are explained, which have been chosen due to the multi-sensor approach. All methods were developed in the German Remote Sensing Data Center of DLR, which has a long-time experience in the field of surface water mask extraction (Martinis et al. 2015b).

RapidMappingFlood (RaMaFlood) is originally for purposes in emergency fast-response mapping, which can be used for all types of available SAR data, and is here applied semi-automatically (Martinis et al. 2015b). By this method all products of the sensors Envisat ASAR and ALOS PALSAR, both provided by open source ESA Earth Online, and ALOS-2 PALSAR, accessed on JAXA AUIG2, were processed (first column of figure 7). After the preprocessing via SNAP, including a radiometric calibration to sigma naught (dB), speckle filtering and geometric correction (Li and Yang 2015; Oliver and Quegan 2004), the individual scenes are

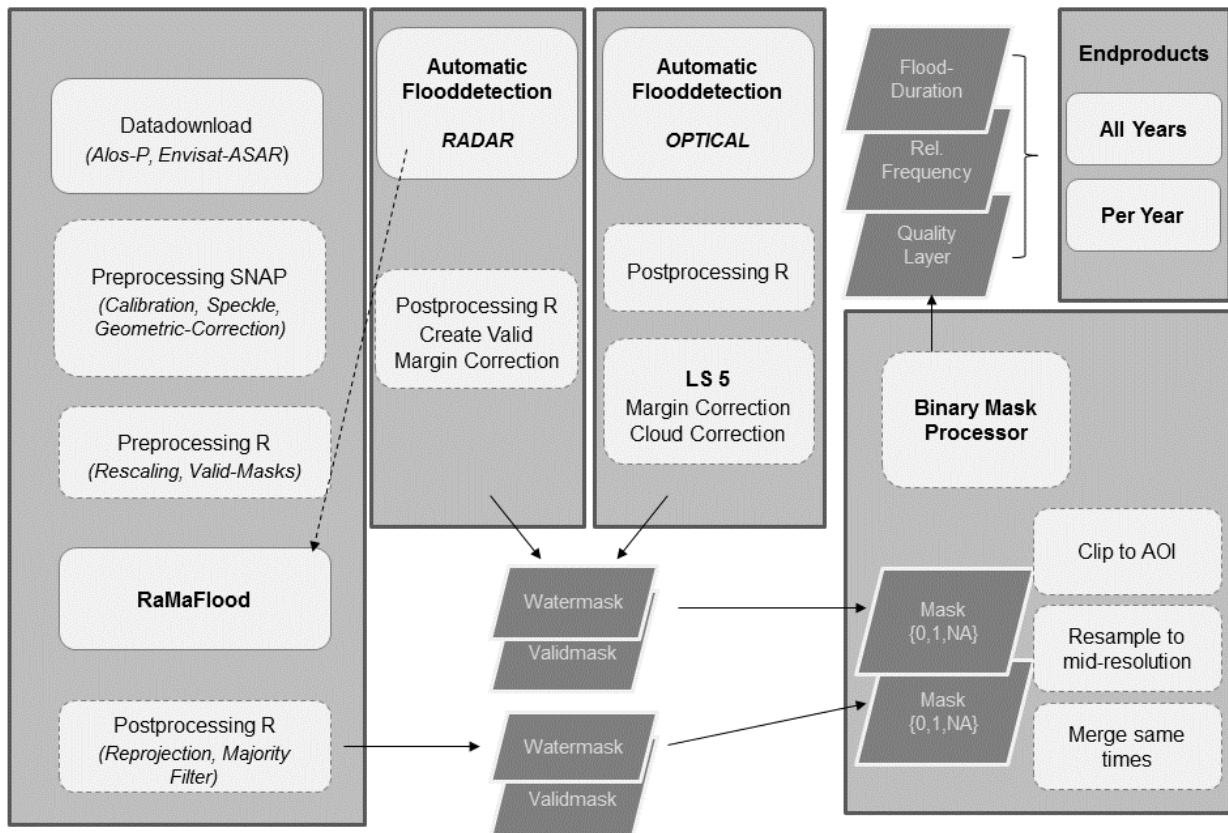


Figure 7: Flowchart of processing

prepared as input data for the RaMaFlood-Tool. This corresponds to a reprojection to UTM, rescaling of the value range from -40db to 0db to 0 to 400 and clipping to the extent of the study area. During preprocessing, valid masks are also generated, which binary differs between the valid and invalid pixels and will be used later. The RaMaFlood processor is based on image segmentation, thresholding for initialization of classification and subsequent post-classification within the e-Cognition Developer software (Martinis et al. 2015b). Because of often low contrast between water and non-water areas and resulting unimodal histograms of the scenes, especially in L-band, a relatively fine uni-scale segmentation and manual thresholding is selected (Martinis et al. 2009; Martinis 2010; Martinis et al. 2011; Martinis et al. 2015b). Finally, a binary majority filter is applied to from L-band derived water masks and all masks, both water and valid, were transformed back to WGS84 to be used later as input for further processing.

The fully automated processing chain of Sentinel-1 based flood mapping (part of the second column for *RADAR* in figure 7, p.27) developed by Twele et al. 2016 is designed for ground range detected Sentinel-1 data in interferometric wide swath mode. Due to its systematic and continuous sensing in VV and VH polarization, Sentinel-1 and its fully automatic processing is well suited for rapid mapping in emergency cases as well as for continuous monitoring of surface water dynamics (ESA 2019b; Twele et al. 2016). The automated processing chain used in this study includes SAR data preprocessing, initial classification using automatic thresholding, fuzzy-logic-based classification refinement and final classification including auxiliary data (Twele et al. 2016). The Sentinel-1 datasets for this analysis are selected manually and downloaded via the Alaska Satellite Facility. Preprocessing is necessary by removing the margin areas of the scenes, which strongly influence the results. Due to the use of an automatic (Martinis et al. 2009), overestimation of water areas occurs especially in the late dry season, where the histograms are not bimodal due to the small flooded areas. In these cases, an analysis was repeated semi-

automatically with RaMaFlood. Using the output data of the automated processing chain, valid masks can be subsequently created for each corresponding water mask.

Like the methods described so far, the fully automated TerraSAR-X flood service (part of the second column for *RADAR* in figure 7, p.27) has also been developed for real-near time flood detection in context of rapid disaster management by Martinis et al. 2015a. The processing of the data contain similar steps to the Sentinel-1 based flood service and was validated as effective and robust on several study areas worldwide (Martinis et al. 2015a). The used TerraSAR-X scenes acquired in the ScanSAR, Stripmap and Spotlight modes are accessed via the EO-Web provided by DLR (Airbus Defence and Space 2015; Buckreuss et al. 2008). Based on the output data, valid masks are created, and margin corrections are performed on error-affected results.

In order to achieve a high spatial and temporal resolution at monitoring hydrological phenomena, Wieland and Martinis 2019 developed a modular processing chain for automated flood monitoring from multi-spectral satellite data (part of the third column for *OPTICAL* in figure 7, p.27), complementing the previously SAR data-based flood services. As it is focused on images with high spatial resolution and large swath widths, it is applied in this study for optical Landsat 5 and Landsat 8 images. By pooling the raw images with several water relevant products (for example the Normalized Differenced Water Index) convolutional neural networks enable a precise water detection at every geography and any time. Already within the processor, the additional classification of clouds, shadow, land and snow leads to the creation of valid masks. Due to margin errors and misclassifications in the area of clouds and cloud shadows, especially in cirrus clouds, the masks derived from Landsat 5 must be modified subsequently (Wieland and Martinis 2019). By an additional water probability layer, the threshold value could be increased for the affected scenes and the valid mask could be modified accordingly.

3.3 Reprocessing of Water Masks

Since a method for combining and reprocessing an aggregation of these water masks (*Binary Mask Processor* in figure 7, p.27) was developed by Shakya 2018 in cooperation with DLR, only the basic principles of the calculation and individual changes are outlined below. All processing described in this sub-chapter (input, data preparation, multi-processing using parallel processing for the central computation, and output generation) is done with python 3.x within the Anaconda environment.

All input files are prepared independently of the original satellite in order to have the same data structure. Sorted by sensor for each scene there is a folder named after the time of recording in date and time, which contains its water mask and the corresponding valid mask, all in WGS84. In addition, there is a shapefile which shows the extent of the study area (Shakya 2018)

This input data is then prepared for analysis as followed: First, the binary water and valid masks are merged, which is originally not included in the processing chain of Shakya 2018. This results in one summarized layer per scene with three values, from 0 as no water, over 1 implying water up to 2, which describes invalid pixels (Skakun et al. 2014). This is followed by a clipping of all scenes onto the investigation area, as well as the spatial merging of several sensor-like scenes within one day to one overflight. Despite the same data structure, the individual images differ greatly in their spatial resolution. To be able to start common calculations, all layers must be aggregated to a common pixel size (Shakya 2018). To keep the change of the individual scenes as small as possible and to ensure greater confidence in the spatial resolution of the results, the scene with the smallest deviation from the arithmetic mean of the pixel size of all overflights is selected and serves as the basis for a subsequent resampling. This is also different from Shakya 2018, where all scenes are brought to the highest available resolution. At the same time, the spatial extent and origin of each raster layer is adjusted to the study area for the exact overlapping of the pixels.

The core calculation runs, as described in Shakya 2018, in three parallel processes. In this study it is not necessary to calculate an optional backward duration for a specific flooding, as the analysis is not event-based, but is intended to capture seasonal dynamics over a whole year (Shakya 2018). The aggregation of all water masks per investigation period, in order to extract several hydrological-related products, is done according to the following principle:

By considering one temporal stack of a georeferenced pixel p through every different scene s within the total amount of scenes n of one investigation year y (figure 8, p.32), different composition of the three possible values $p=0$ (no flood), $p=1$ (flood), $p=2$ (invalid) create the following output layers for each investigation period: ‘Relative Frequency’ (relFreq), ‘Total Duration’ (TD) and the ‘Quality Layer’ (QL) QA, QB and QC (figure 7, p.27). All calculations are made pixelwise for one georeferenced pixel p and do not include any neighbor. Therefore, no spatial variables for the x and y coordinates are given in the equations and the geospatial raster is just a matrix output format for all pixels. The only dimension is a temporal stack of p_s for the year y with its corresponding sum of overflights n : The relFreq (equation 1, p.32) is the proportion of the amount (frequency = F) of flooded pixels ($p=0$) per sum of valid observations ($p=0$ OR $p=1$) (Pekel et al. 2016; Shakya 2018; Skakun et al. 2014; Tulbure et al. 2016). The TD (equation 2, p.32) is the sum of the days between two consecutive water observations. These periods of days are named t_h as a part of all flooding periods k . The QL QA, QB and QC from Shakya 2018 are also used. Layer QA (equation 3, p.32) is the sum of the days between the last non-water occurrence before a flood and the first water pixel, included in a flooding period t_h , represented as a_i out of all pre-flood periods l . Layer QB in turn (equation 4, p.32) records the days for the transition time between the last water pixel of a flood to the first non-water pixel. Hereby it captures the post-flooding periods b_j out of all such time spans m . QC (equation 5,

p.32) in turn indicates the density for p of valid flood observations (FO), multiplied with 100, to the TD of the corresponding pixel (Shakya 2018).

$$relFreq_y(p) = \frac{F_{yn}(p_{ys} = 1)}{F_{yn}(p_{ys} = 0) + F_{yn}(p_{ys} = 1)} \quad (1)$$

$$TD_y = \sum_{h=1}^k t_h \quad (2)$$

$$QA_y = \sum_{i=1}^l a_i \quad (3)$$

$$QB_y = \sum_{j=1}^m b_j \quad (4)$$

$$QC_y = \frac{F_{yn}(p_{ys} = 1) * 100}{TD_y} \quad (5)$$

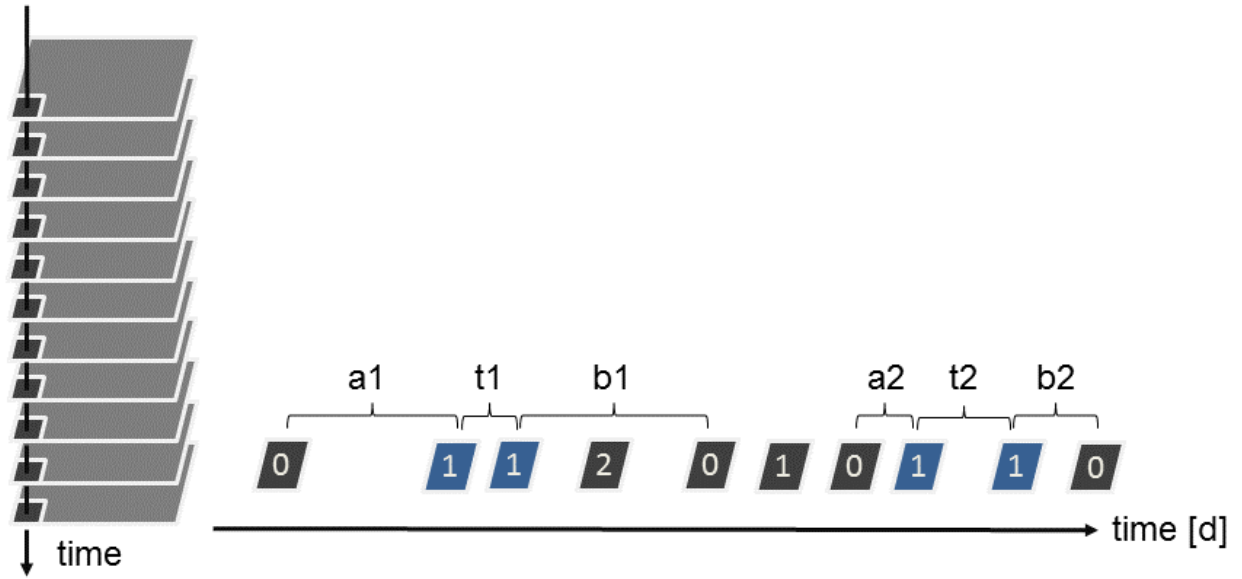


Figure 8: Visualization of the Binary Mask Processor

3.4 Product Processing

The previous output layers serve as the basis for calculating further results. Here, analyses can be carried out both on an annual level and on a temporally aggregated level over all three years of investigation (figure 7, p.27). All methods described here are applied by open source software RStudio.

The additional results per investigation period include a layer for the 'Number of valid Observations', a mask of 'Permanent Water', the 'Maximum Water Extent' (MWE) and a statistical 'Frequency Distribution' of the TD. As a by-product of the relFreq, the 'Number of valid Observations' (denominator in equation 1, p.32) can additionally be generated as output, which provides information about annual and spatial differences in data density. Furthermore, the definition of Pekel et al. 2016 is used to differentiate between permanent and flooded water surfaces in order to be used as masks for the result layers. Since one year with 365 days is not completely covered in time (figure 3-5, p.22-24), all water bodies are defined as permanent, where the number of days with water presence within the TD layer is higher than the maximum possible number of days minus 30 (Pekel et al. 2016). Although MWE layers are also considered by Pekel et al. 2016, Skakun et al. 2014 and Tulbure et al. 2016, in their analyses they only take at least one observation of water through the investigation period as a prerequisite. This is a crucial difference to the method used here, where only those areas are included in the MWE, that are covered by water for at least one day and thus require at least two consecutive water observations. Furthermore, a slightly generalised 'Frequency Distribution' of the TD is drawn up for every study year in order to identify possible patterns in a later annual comparison.

Additional to the results per investigation period, temporally aggregated layers over the three investigation years y are calculated. This contains simple reclassifications as well as statistical statements about the inter-annual means and variabilities of the floods. General summaries of the layers 'Permanent Water' and MWE are achieved by the following reclassifications: While

water surfaces are only overall-permanent if their pixels are classified as permanent over all years, the aggregated MWE is divided into three categories of water occurrence (WO): once, twice or three times (Long et al. 2014; Skakun et al. 2014). In addition to this, statistics on averages \bar{A} (equation 6 and 7) and variability $relRange$ (equation 8a and 8b) are determined for the $relFreq_y$ and TD_y over the investigation periods. As $relFreq_y$ and TD_y represent one value of the georeferenced pixel p , mathematical calculations can be expressed with the only variable y in time dimension. Here the methods of averaging differ. While for TD the only possible way is a calculation of the arithmetic mean (equation 6), for $relFreq$ a new overall frequency over all scenes yn of every investigation period y is formed (equation 7), which in turn results in a resampling of all scenes for joint calculation.

$$\bar{A}_{TD} = \overline{TD_y} \quad (6)$$

$$\bar{A}_{relFreq} = \left(\sum_{y=1}^3 F_{yn}(p_{ys} = 1) \right) / \left(\sum_{y=1}^3 F_{yn}(p_{ys} = 1) + \sum_{y=1}^3 F_{yn}(p_{ys} = 0) \right) \quad (7)$$

However, the calculation of the variability is done in the same way for both layers (equation 8a, b). Per georeferenced pixel it contains the averaging \bar{A} in the numerator and the absolute range ($max - min$) of the result layers over the three investigation years y in the denominator. By this combination, the probability and variability of the occurrence of water is taken simultaneously into account.

$$relRange_{TD} = \frac{\bar{A}_{TD}}{max \{TD_1, TD_2, TD_3\} - min \{TD_1, TD_2, TD_3\}} \quad (8a)$$

$$relRange_{relFreq} = \frac{\bar{A}_{relFreq}}{max \{TD_1, TD_2, TD_3\} - min \{TD_1, TD_2, TD_3\}} \quad (8b)$$

While layer QC (equation 5, p.32) is taken unchanged as one of the two QL, layer QA (equation 3, p.32) and QB (equation 4, p.32) are combined to calculate the ‘Number of uncertain Days’ (NUD). Based on the simplifying assumption that the flood begins (layer QA) or ends (layer QB) in the middle between a flooding and a non-flooding period, both are divided by two and added for displaying the sum of days where water could additionally be present but is not captured (equation 9):

$$NUD_y = \frac{QA_y}{2} + \frac{QB_y}{2} \quad (9)$$

4 Results

The aim of this chapter is to describe the results obtained by applying the methods described so far. The focus is on the results of three hydrological-related products: The ‘Maximum Water Extent’ (MWE), the ‘Relative Frequency’ (relFreq), and the ‘Total Duration’ (TD) of flooding. The order of the products simultaneously implies an increase in the information content within the inundation areas, from the mere water occurrence (WO) within one year up to the temporal dimension within the inundated areas. A subsequent further view on the respective ‘Frequency Distributions’ of the TD for the investigation years widens the analysis. At least two different ‘Quality Layers’ (QL) regarding the hydrological products provide an alternative to a common validation. Because of the presentation of the whole large study area, differences in the spatial distribution over the Iishana Zone can be better seen in the maps than the results around various distinct flooded areas. This is rather a problem of visualization and no limitation of the spatial resolution.

4.1 Maximum Water Extent (MWE)

The MWE, shown in figure 9 (p.37) indicates all areas where water has been detected at least one day within the investigation period. Although this layer does not provide information about differences within the floods, it focuses on variations in the spatial extent, distribution and concentration of flooding over the whole study area comparing the three various years A (wet and dry season from 10/2007 – 09/2008), B (wet and dry season from 10/2008 – 09/2009) and C (wet and dry season from 10/2016 – 09/2017). Comparing the sheer extent of the maximum flooded area per year A has the biggest one with nearly 6,000 km² followed by almost 5,500 km² in C and at least a little less than 5,500 km² in B. But this layer becomes more meaningful, however, if the concentration of the flooding is considered. On the one hand in C almost the entire Iishana Zone was affected nearly even, which can be seen especially by the inundated areas in the northwestern center and the northeast of the study area, where the overall extent in A and B is smaller. On the other, spatial concentration of the floods can be found most evidently in the south east of the study area around the Omadhiya Lakes, as you can see also in the zoom sections. Particularly in B, a concentration of flooding to the southeast is most striking. Hence A forms a transition from widespread and evenly distributed flooding behavior in C to a more concentrated but smaller flooding in B.

The temporally aggregated layer in the last row of figure 9 (p.37) shows the years of WO per pixel. 41.7 % of all flooded pixels are only flooded in one year, while 32% were covered with surface water through all three years of investigation and in at least 26.3% water was detected in two years. The contrast that more than 73% were either once or always covered by water shows at the same time a high variability of water recurrence, especially in the northwestern parts, as well as a clear pattern of water bearing drainage systems during a flood, particularly in the more southeastern regions of the study area.

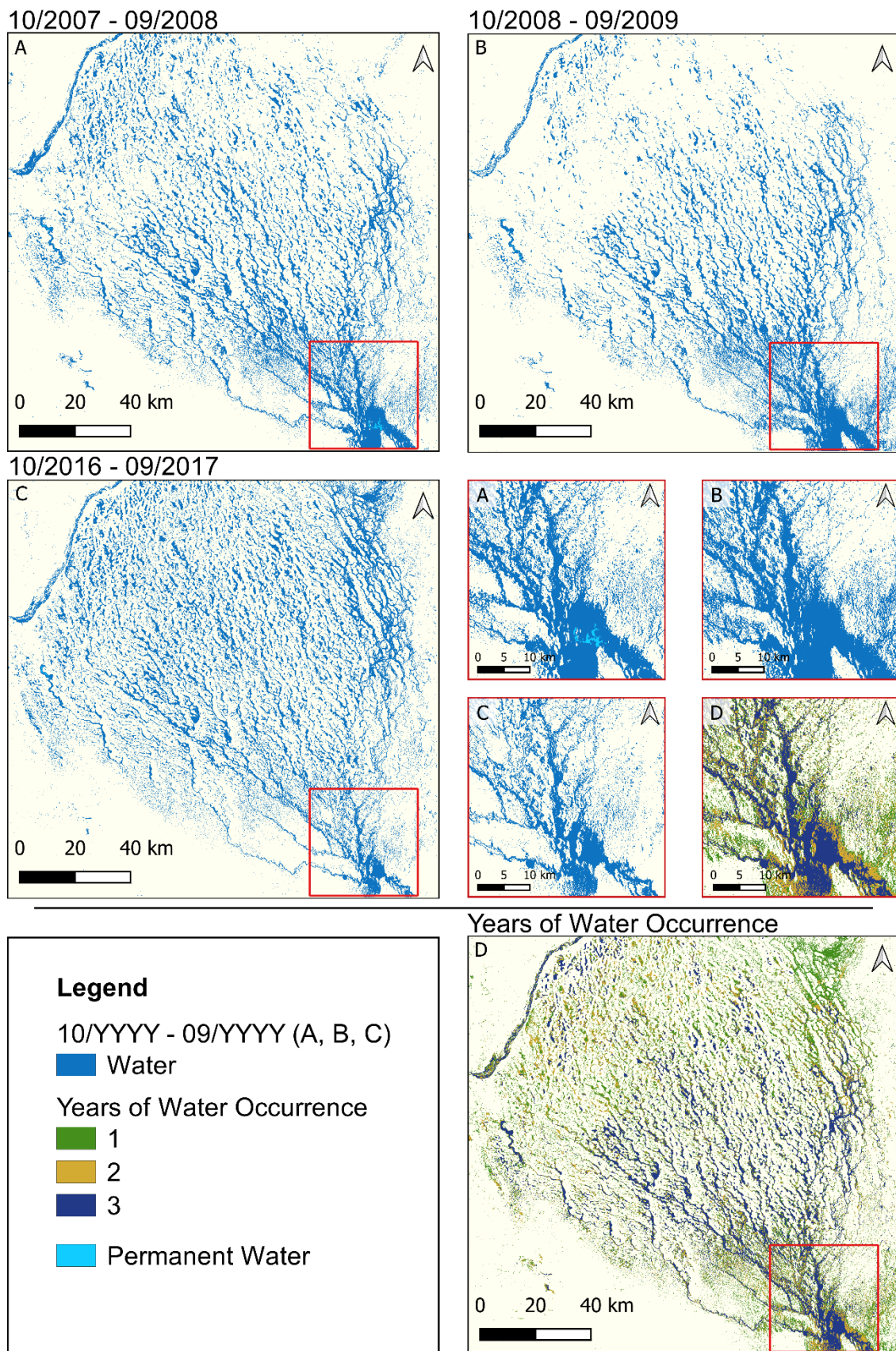


Figure 9: 'Maximum Water Extent' for each year (A, B, C) and their mean and relative range (D), as well as corresponding zooms. Background color does not imply any data.

4.2 Relative Frequency (*relFreq*)

Figure 10 (p.39) shows the *relFreq* of the three investigation periods and two over the years aggregated layers. All layers, except the 'Relative Range of relative Frequency', reflect the proportion of WO to the sum of all valid observations. On this, striking areas can be identified over all three years of investigation in the map of 'Overall relative Frequency' (bottom left). Beside the most northwestern linear feature, the Cunene River, which has a separate catchment area and no drainage influence to the Iishana Zone (Mendelsohn et al. 2013), the Omadhiya Lakes in the southeast (visible also in the zoom sections) and the Olushandja Dam in the west are recognizable among the areas with the highest values of the *relFreq*. In addition, the more variable *iishana* can be seen distributed all between these striking features and seem to flow into the Omadhiya Lakes. Regarding these channels and pans of the Iishana Zone the following general pattern can be assumed. The more southeastern surface water occurs, the more close, linear and connected the network becomes and the more northwestern, the more separated, individual and smaller are inundation areas in contrast. Despite these overall similarities, clear differences can be seen between the investigation periods. It is apparent that the *relFreq* in A and B show a larger area of higher values in comparison to C and therefore the linear and oval waterbodies in A and B form a more holistic image of the drainage network, while in C the oval water feature can be seen more clearly.

The 'Relative Range of relative Frequency' (bottom right) combines the general probability of spatial WO, represented by the 'Overall relative Frequency', with their temporal variability, expressed by the absolute range. The lower the values the more probable and stable is the recurrence of surface water on this pixel. Here you can see especially larger connected areas, forming clear features with a higher probability of recurrence. In contrast the very small punctual points around the Omadhiya Lakes in the southeast nearly form a diffuse area of surface water, recurring very unstable over time. These unstably flooded areas can be found

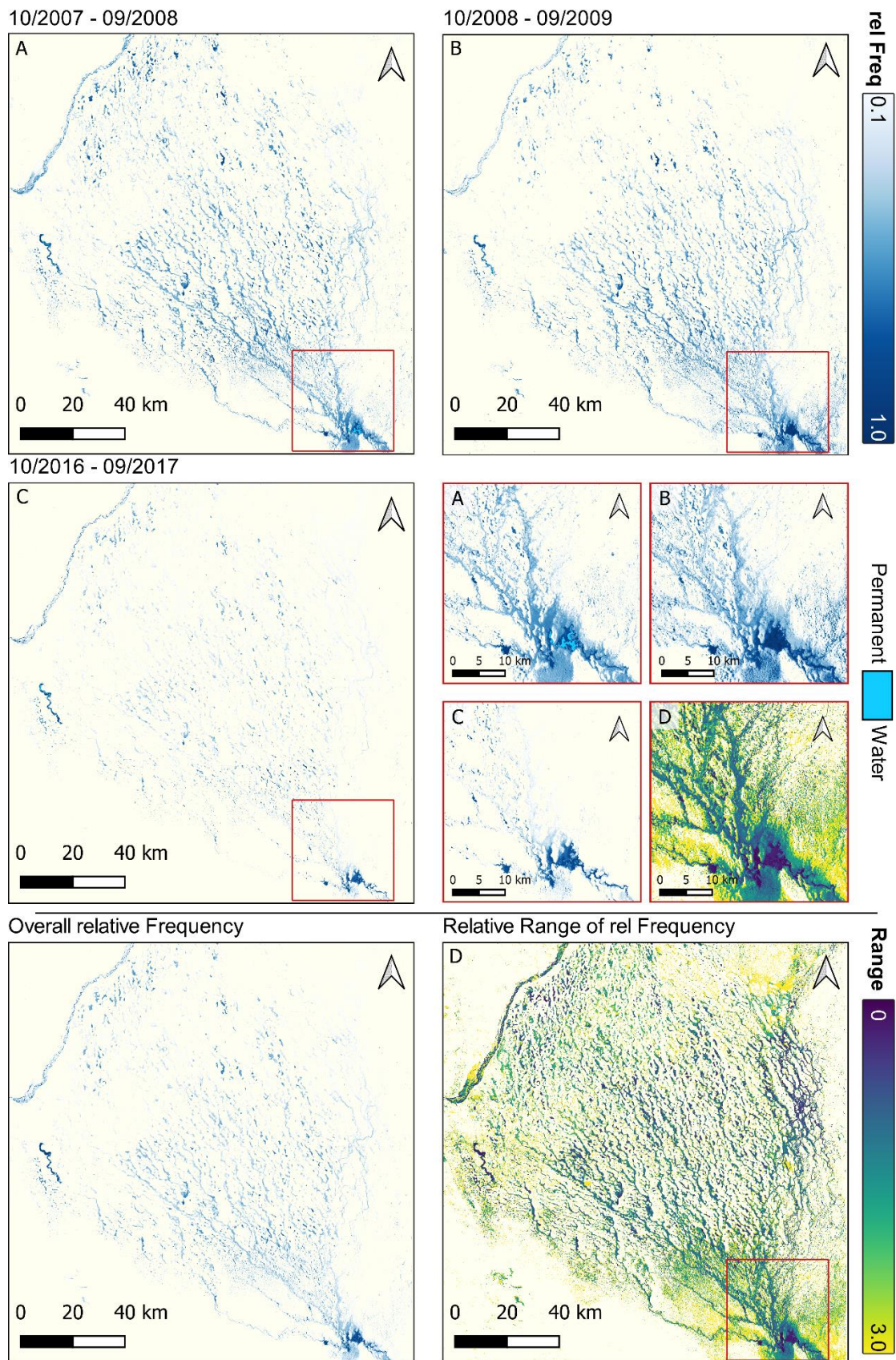


Figure 10: 'Relative Frequency' for each year (A, B, C) and their overall and relative range (D), as well as corresponding zooms. Background color does not imply any data.

supplementing on smaller extents in the northwest and the north, where the differences between the years were already evident within the MWE layers

4.3 Total Duration (TD)

The TD layer shows the sum of all inundated days per pixel (Shakya 2018). Like the relFreq, the maps in figure 11 (p.41) also show two different levels of content, the three annual investigation periods and the two temporal aggregated layers. It is in general evident that most areas are flooded on average only briefly over a few days. Sites affected by a longer flooding period coincide with the striking feature of the relFreq (for example the Omadhiya Lakes and Olushandja Dam) and area often more oval than linear. After the differences in the overall spatial distribution were described previously, the main contribution of the TD is to point out the variability within the inundation areas. Therefore, the different complexities of flooding become evident, as an example especially in the zoom sections. Here it is noticeable that only very few areas have permanent surface water, as defined by Pekel 2016. While the striking areas of generally longer inundation duration at Omadhiya Lakes have nearly the same spatial outline over the years, they differ in their temporal dimension. In A the biggest part of permanent water can be found in the east of the Omadhiya Lakes. Additionally, surrounding lakes are inundated several months and their broader transition areas over a few weeks. While in B the sheer extent of flooding is bigger, the most eastern lake has no permanent water but a surface WO of a few months. The enclosing areas, which were flooded over several months in A, just have flooding durations of a few weeks. Also C has its own pattern: Comparing the spatial extent it is clearly the smallest of all investigation periods and as well as in B no areas are flooded permanently. But in contrast there is no special lake which stands out with a higher inundation period and the duration of flooding with a few months is in terms of area bigger than in B.

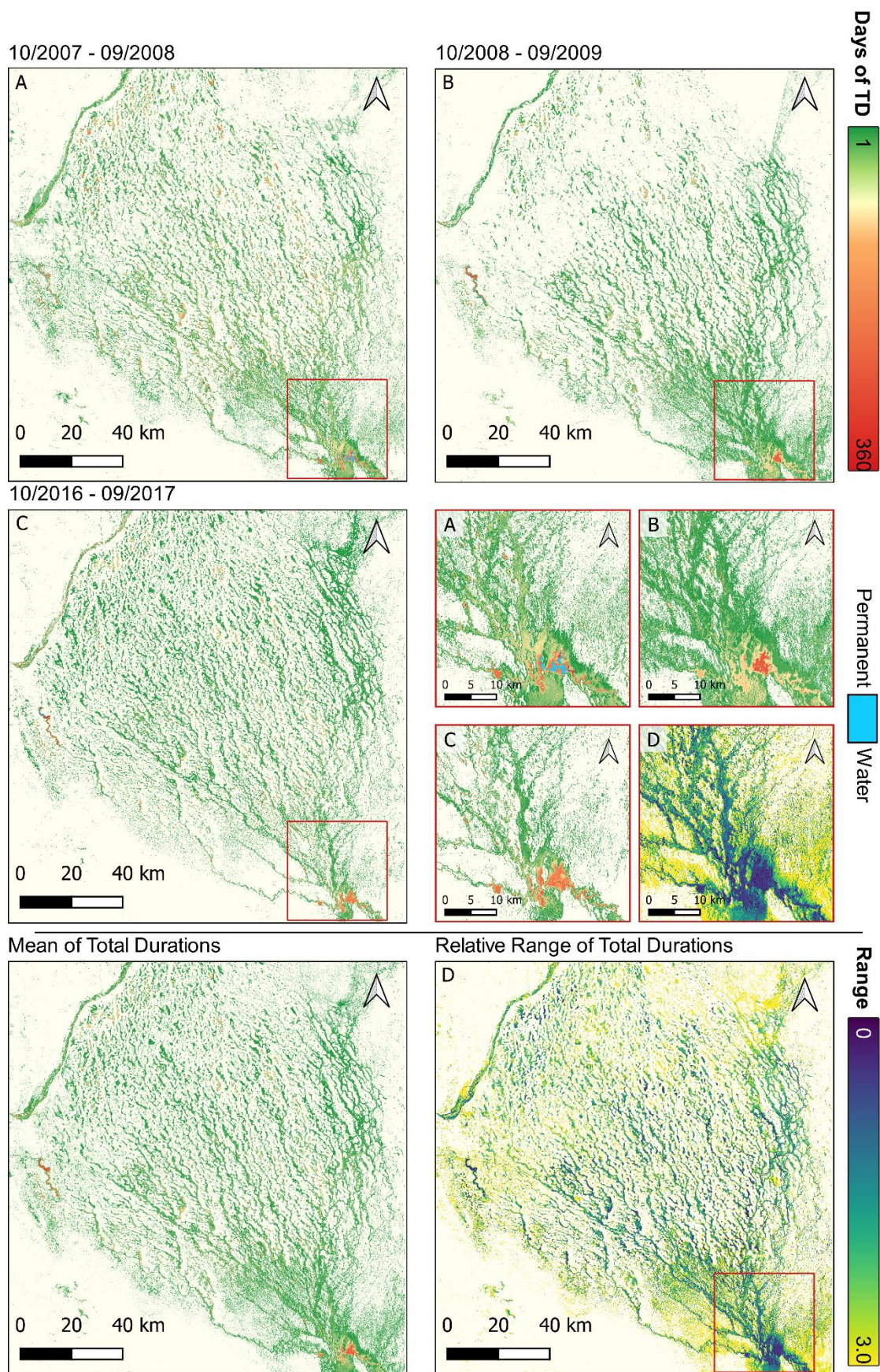


Figure 11: 'Total Duration' for each year (A, B, C) and their mean and relative range (D), as well as corresponding zooms. Background color does not imply any data.

Regarding the two aggregated layers in the last row of figure 11 (p.41), there are in general almost none areas at all which are covered permanently through every year (except a few non-visible pixels inside the Olushandja Dam), but the 'Relative Range of Total Duration' clearly distinguishes the stably flooded areas with a high rate of surface water recurrence to the surrounding variable and less likely inundated areas. Recognizable patterns are the same as in the 'Relative Range of relative Frequency' (figure 10, p.39). Considering the temporal dimension of a flooding given by the TD, a rising complexity within the inundated area is therefore evident.

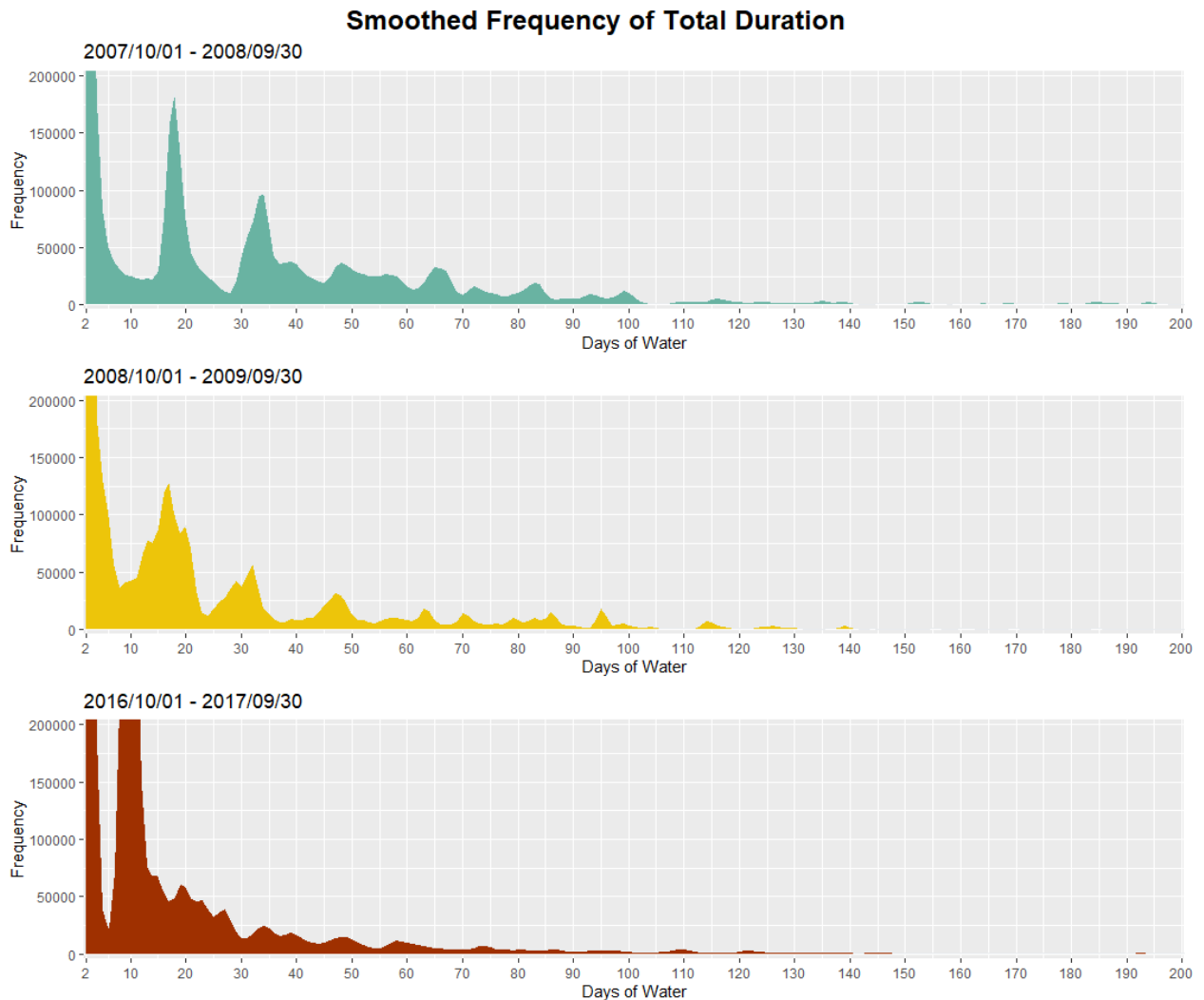


Figure 12: Comparison between the 'Frequency Distribution' of 'Total Duration' of the three investigation periods

Figure 12 (p.42) compares the ‘Frequency Distributions’ of the TD layers between the hydrological years. The spatial and temporal differences in the origin and the courses of these flood years limit the comparability of the observed periods. Nevertheless, similarities are discernible, especially between the first two investigation years. In general, a strong decrease of the absolute frequency can be observed with increasing flooding time and from about 100 days on, only sporadically insular flooded areas can be found. The three years are also connected by a striking low within the first days. But here a temporal shift is visible. While in 2016/2017 the frequency collapse appears already at about 5 days, in 2008/2009 this dip is noticeable shortly before 10 days and in 2007/2008 clearly after 10 days. Comparing the first two investigation periods a pattern of three peaks becomes clear, but a geographical mapping of the common peaks did not reveal any spatial coupling. The reasons for such distribution can therefore be of a general nature, which will be further responded to in the discussion.

4.4 Validation

Since the DLR methods for generating the various water masks are already validated, the focus is on a quality assessment of the previously declared output products. Although emergency maps for fast response (ICSMD 2009; ZKI 2008, 2009) could have been used for the validation of single flood masks, but it would not represent the quality of the output layers, also because these maps work in the same rapid mapping context as the DLR methods do.

You can find the validation of the four methods as followed: RaMaFlood in Martinis et al. 2015b, the fully automated TerraSAR-X based flood service in Martinis et al. 2013 and Martinis et al. 2015a, the fully automated processing chain for Sentinel-1 based flood mapping in Twele et al. 2016, and the modular processing chain for automated flood monitoring from multi-spectral satellite data used for Landsat in Wieland and Martinis 2019.

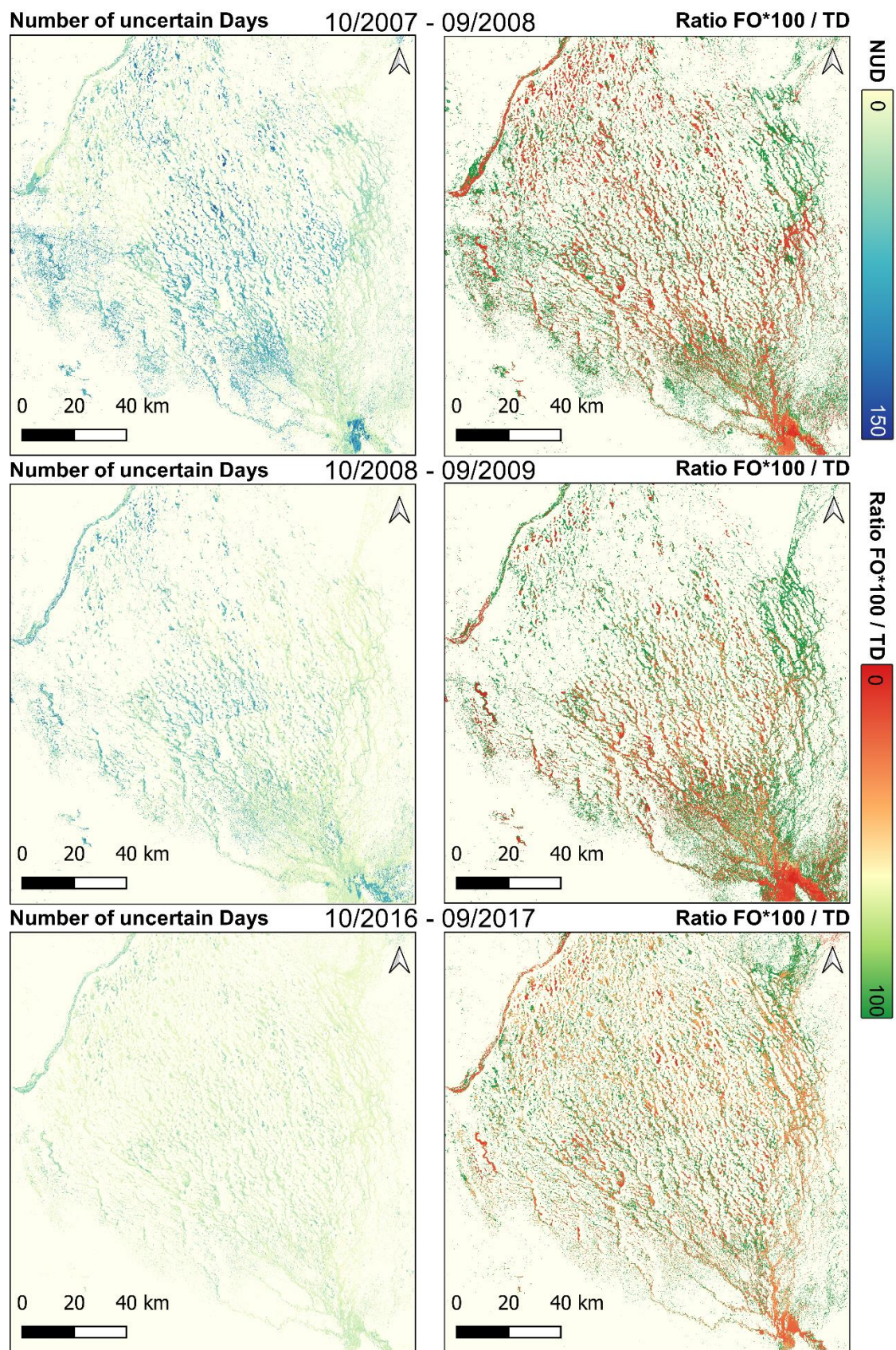


Figure 13: Two 'Quality Layers' for each year, including the 'Number of uncertain Days' and the Ratio 'FloodObservations(FO) * 100 / TD'

Because the MWE and the relFreq just represent the information of the flood masks without deriving another dimension or information level, no specific validation is performed here, but certain error susceptibilities can be found in the discussion part. As no similar product like the TD is available for the study area, no common validation of this product can be done. Therefore, the QL from Shakya 2018 are used and slightly modified.

Figure 13 (p.44) shows two layers for each investigation period. The ‘Number of uncertain Days’ (NUD) depicts the transition periods within the unit of days between a beginning or an end of flooding to its prior or subsequent valid observation of no surface water (Shakya 2018). It now indicates all days, which might have been erroneously not detected as floods. When comparing the three investigation periods, the lower underestimation of flooding in 2016/2017 is thus clearly evident. While in general larger areas of high values of the NUD can be found in 2007/2008, both 2007/2008 and 2008/2009 are less affected in the east.

It is also necessary to take the vulnerability to possible overestimation of days during flooding periods into account. The longer the time intervals between two consecutive FO, the higher the probability that areas that have dried up and flooded again will not be detected (Shakya 2018). This is observed by the ‘Ratio FO * 100/ TD’. The higher the ratio between the valid FO and the TD, the finer and more reliable is the flooding period in days. While generally higher values can also be found here in 2016/2017, in combination with the TD it can be seen over all three periods that the longer areas are flooded, the less precise the duration in days becomes, which can be seen in the example of the Omadhiya Lakes.

5 Discussion

The aim of the chapter is a critical analysis of the selected data, methods and results. In the subchapter ‘Multi-Sensor Satellite Data for Derivation of Surface Water Products’, the selected

multi-sensor approach and the data used for water detection are discussed first, followed by the advantages and disadvantages of the processing, strengths and weaknesses in the interpretation and quality of the derived products. A more general interpretation of the results in the context of the hydrological system of the Iishana Zone can be found in the subchapter of ‘Surface Water Dynamics of the Iishana Zone’.

5.1 Multi-Sensor Satellite Data for Derivation of Surface Water Products

While in many studies complex issues are solved by simultaneous multi-modal observations, the selection of several satellites in this study is primarily used for temporal supplementation and secondarily for content complementation (Töyrä et al. 2001). Therefore the main reason for choosing a multi-sensor approach is the simple increase in temporal data density (Mizuochi et al. 2014), and therefore the different products do not flow together in one data pool for the creation of single water masks. So the input datasets contain different and above all complementary information of the land surface (Töyrä et al. 2001), which avoids the specification of a certain bias, but at the same time increases the variety of reasons for error susceptibility.

Different processes thus standardize the input data from variable sensor of variable acquisition modes with respective advantages and disadvantages to general common water masks (Long et al. 2014; Martinis et al. 2015b). Within the various radar sensors, for example, the wavelength plays a particularly important role. While at shorter wavelengths (X-band for TerraSAR-X) the contrast between different land cover, such as between sand and water, is more pronounced (Williams and Greeley 2004) in comparison to longer electromagnetic pulses (L-band for ALOS(2)-PALSAR) which in turn are less susceptible to slight roughness on the surface, such as smaller water waves or water plants (Martinis et al. 2015b). Differences between the sensors becomes even clearer when comparing optical and radar data. Here, two physically completely different approaches of obtaining land surface information lead to the extraction of water masks.

With optical sensor systems only the spectral reflection values of the surface are observed, whereas radar can penetrate deeper into the cover with increasing wavelength (Jensen 2016). This has a strong effect on the detection of vegetation-covered water surfaces. While in optical data the vegetation is dominant and it cannot be distinguished between flooded and non-flooded vegetation (Mizuochi et al. 2014; Pekel et al. 2016; Skakun et al. 2014; Töyrä et al. 2001; Wieland and Martinis 2019), in radar data it is possible to detect water under vegetation due to an enormously increased backscatter signal caused by the double-bounce effect (Long et al. 2014; Martinis et al. 2015b). Since the analyses are carried out both during rainy and dry seasons, seasonal vegetation on water surfaces varies greatly. By only observing open surface water, also with radar data, flooded areas are indeed underestimated, especially during the late rainy season, when the vegetation is richer and linked to presence of water. But at the same time this leads to a content-related and methodical contingency of water detection. Due to the multi-sensor approach and a necessary comparison between the optical- and radar-derived water masks, it is therefore not considered necessary to detect flooded vegetation with SAR satellites.

Furthermore, in processing there are many steps between the original data and the unified water masks, including data download, preprocessing, water mask generation and the respective post-classification (Martinis et al. 2015a; Martinis et al. 2015b; Twele et al. 2016; Wieland and Martinis 2019). The higher the variety of different remote sensing products used in a study, the more different the individual processing steps become (Long et al. 2014). A resulting decrease in automation (Martinis et al. 2015b) and several manual interventions increases therefore the susceptibility to errors and the risk of decreasing comparability. As an example, six different data portals are required to download the 12 remote sensing products (table 1 and 2, p.20). Also the use of four different methods for the derivation of the water masks show strong differences: In contrast to the fully automated processing chains for Landsat (Wieland and Martinis 2019) as well as for Sentinel-1 (Twele et al. 2016) and TerraSAR-X (Martinis et al. 2015a), RaMaFlood

(Martinis et al. 2015b) relies on the expertise of the user through manual thresholding. Again, the resulting water masks must in turn be treated differently to provide a standardized input for further reprocessing within the *Binary Mask Processor* (figure 7, p.27). For example, this is noticeable even within same processing chains, since water masks of Landsat 5 and Landsat 8 are both derived with the method of Wieland and Martinis 2019 for multi-spectral satellite data. While the Landsat 8 masks can be used directly as output from this automated processor, Landsat 5 requires a margin correction and in case of heavy cirrus clouds a complete manipulation of the water and valid masks. Subsequent reprocessing within the *Binary Mask Processor* also changes the data quality of the unified water masks. By reprojecting and resampling to a common pixel size, the spatial precision of the pixel location decreases (Long et al. 2014). In summary the multi-sensor approach combines different strengths and weaknesses of the sensors for water detection, which compensate each other and thus make the analysis more robust against biases. But also the spatial accuracy becomes less by the separated water mask generation and the subsequent unifying process (Persendt and Gomez 2016; Töyrä et al. 2001).

By continuing with the susceptibility to these problems during further processing, spatial accuracy as well as the size of the scenes and their effects on the result layers must be considered (Long et al. 2014; Skakun et al. 2014; Tulbure et al. 2016). Since each overflight has a different position and coverage of the study area, observations within one investigation period are made with different frequencies and time variations per georeferenced pixel in comparison to its neighbors. This influences the comparability of individual pixels within a result layer, which is also expressed by the QL per year (figure 13 p.44) or the ‘Number of valid Observations’ (figure 14, p.50). Therefore both, the first and the last image of one investigation year should cover the entire study area to ensure a comparability between the maximum time frame as a common base for calculating the TD (Shakya 2018).

Additionally, the comparability of the respective results between the study years is strongly influenced by the temporal resolution of the overflights per year. The MWE is most affected by these restrictions. Its accuracy compared to actual flooded areas can be distorted due to the strong dependence of the time of sensing (Skakun et al. 2014). However, due to the activation of the Center for Satellite Based Crisis Information (ZKI) of DLR in mid-March 2008 (ZKI 2008) and the International Charter Space and Major Disasters (ICSMD) at the end of February 2009 (ICSMD 2009; ZKI 2009), there is an increased repetition rate of observations during acute flood emergencies (figure 3 and 4, p.22 and p.23). This concentration of observations also influences the relFreq (figure 10, p.39), as there is now a higher data density and therefore a higher frequency of observations during heavy flooding. This now shows in turn the strength of the calculation of the TD. By considering the time dimension, the floods get a kind of equalization of the data density. For a risk assessment this is of great value because not only the spatial extent but also the duration of the flooding indicates its severity (Awadallah and Tabet 2015). However, the used method for deriving the TD contains a general bias of underestimating the flooding times, as water probably occurs before and after the clear detected flooding periods, which is shown by the NUD in figure 13 (p.44). At the same time, there is a risk of overestimating the duration during periods of less observations particularly during the dry season, which is the reason for the correlation between long flooded areas in the TD and low values in QC.

While in the ‘Data and Methods’ section the temporally different distribution of images within a year was already mentioned (figures 3-5, p.22-24), figure 14 (p.50) shows the general difference in the frequency of valid observations. A comparison between 2007/2008 and 2008/2009 shows the importance of considering both, the general amount of valid observations and the quality of the layer. Although 2007/2008 has a slightly better general coverage of overflights than 2008/2009, its NUD values are significantly higher (figure 13, p.44), which

implies a higher error. This is caused by a broader temporal distribution of scenes over the year 2007/2008 including also observations during the dry season (figure 3, p.22). In contrast, 2008/2009 has a concentration of observations during the flood event within the rainy season and very less during the dry season (figure 4, p.23), which explains the lower values for NUD, but at all a worse temporal coverage over the whole year (figure 14). Furthermore, a strong increase of data in 2016/2017 may be the clearest statement of figure 14, which proves that 2016/2017 (represented by map C in the previous figures of the ‘Results’ chapter) is hereby the most reliable year. The reason therefore lies in an enormous rise of data availability due to the ESAs Copernicus Program. ALOS-2 PALSAR is almost obsolete in the analysis of 2016/2017 and the publicly available missions of Landsat 8 and Sentinel-1B dominate the data density (figures 5, p.24). This potential can be further increased by the inclusion of the multi-spectral and optical Satellite Sentinel-2 (Wieland and Martinis 2019).

5.2 Surface Water Dynamics of the *Iishana* Zone

In the following, the individual results of the study years are now interpreted and general statements about the hydrology of the study area are drawn up. In the ‘Results’ chapter it became clear that each period of investigation has its own characteristics in the spatial extent and the distribution of the flooding. Generalized every year follows its own flood pattern: A = biggest inundated area, B = most concentrated distribution and C = most evenly and widespread flooding. This is also clearly visible for the flooding in 2007/2008 and 2008/2009 in Mizuochi et al. 2014. Due to these annually different characteristics of the floods, the calculation of the arithmetic mean for TD_y is less meaningful than the observation of individual years or the variability layer. It also proves the strong spatial dependence of pluvial floods on the precipitation and its volume, spatial distribution, intensity, and duration of the rainy season (Awadallah and Tabet 2015; Mendelsohn et al. 2013; Mendelsohn and Weber 2011; Persendt 2016; Persendt and Gomez 2016; Persendt et al. 2015). Here, further research linking the distribution of precipitation and the spread of the flood through runoff networks is recommended like in Persendt and Gomez 2016. Even more important is the implementation of a robust and effective hydrological model to predict floods in current emergency situations (Goormans et al. 2015; Mufeti et al. 2013). The flood masks created in this study can be auxiliary used for this purpose (Mason et al. 2016).

Due to the high spatial resolution of 30m, clear connections of the flooded areas can be recognized, which provide information about the drainage network. It can be assumed that isolated larger pans are predominant in the northwest, while in the southeast wide connected run-off channels prevail and are supplemented by numerous isolated mini-pans around the Omadhiya Lakes. Due to this lacking connectivity between the *iishana* in the northwest of the study area the flooding is there more pluvial-driven than in the southeast, where down-flowing upland water and therefore fluvial flooding plays an additional role. This is also confirmed by

the landscape genesis as the northwestern Iishana Zone is said to be longer cut-off from a bigger common drainage system through the CB than the eastern part and therefore in evidence has the most saline soil conditions (Mendelsohn et al. 2013).

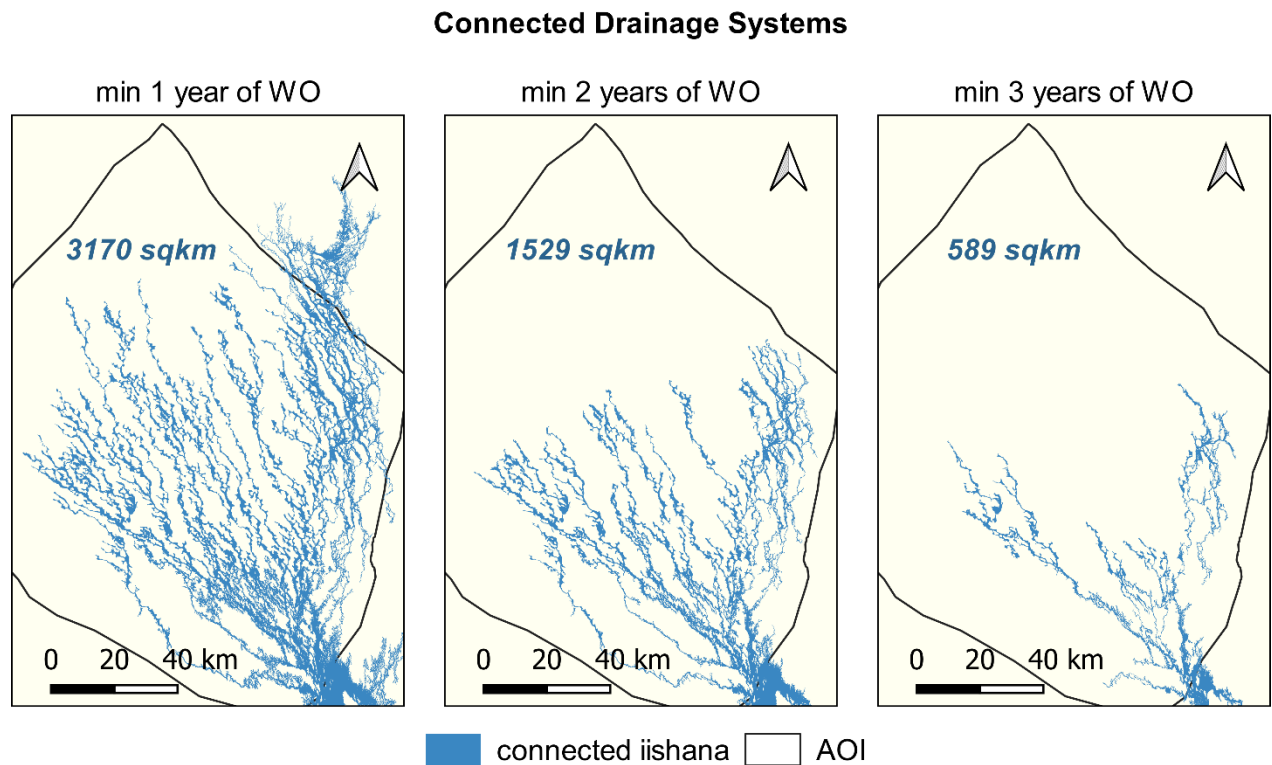


Figure 15: Connected drainage systems in dependence on the years of water occurrence

These assumptions are proven by figure 15, which shows three drainage systems in the Iishana Zone, each flowing interrelatedly into the Omadhiya Lakes. This is a first approach to derive connected or isolated water areas and thus to understand flowing patterns. Therefore the layer 'Years of Water Occurrence' of the MWE is used, split into its three values and reduced to the biggest connected inundated area. On the left side a drainage system can be seen, composed of connected pixels which have been flooded in at least one of the three investigation year. Here linked *iishana* over three quarters of the study area are visible as well as a partially connectivity to the Central Drainage of the CB in the northeast, which can be recognized by its branched channels. But only in unlikely extreme events of very high rainfall, distributed all over the Iishana Zone, all these channels could form together its large catchment area of 3170 km².

Already in the map in the middle of figure 15 (p.52) the connected network is halved to 1529 km². Due to a minimum of two years of WO, this is a more likely representation of the drainage system, which could flow in the Omadhiya Lakes during heavy flooding. On the right in figure 15 (p.52), channels can be seen which join and flow together with a high degree of confidence at almost every flood, but accordingly have only a very small extent of 589 km². This interpretation means that the statements about the hydrology would have to be examined more critically where it is assumed, that flooded areas all over the Iishana Zone regularly form channels and flow off towards the southeast (Awadallah and Tabet 2015; Faulstich et al. 2018; Mendelsohn et al. 2013; Mizuochi et al. 2014). This could only be the case in very extreme events, and then especially in more eastern areas. Therefore, during moderate floods, accumulated water thus distributes worse by the drainage system than previously assumed.

Furthermore, the channels generally have on average shorter flooding durations than the surrounding pans, indicating the drainage effect of the channels and the storage function of the pans of the *iishana*. This can be seen in the figure 10 (p.39), where the most reliable year C shows that especially high values of the relFreq can be seen within oval water bodies. The isolated peaks of significantly longer flooding duration in the 'Frequency Distribution' in figure 12 (p.42) could also represent these particularly large water bodies. This confirms that once connected pans split off the drainage system after a certain time and thus carry water for a longer duration (Awadallah and Tabet 2015; Mendelsohn et al. 2013; Persendt and Gomez 2016). On the contrary, unconnected smaller pans and simultaneously shorter presence of surface water confirm the high infiltration and evapotranspiration rates (Marsh 1992; Mendelsohn et al. 2013). Even more spatial and temporal precise analyses of the drainage system including a derivation of major and minor channels on a smaller scale is recommended and can be carried out on the base of these results.

This strongly varying dynamics within the TD is also shown by the 'Frequency Distributions' in figure 12 (p.42). This is especially underlined by the common high and low within the first few days. This peaks pixel could provide information on the spatial location of the precipitation, since these areas are only flooded for a short time and drain off or infiltrate quickly. However, their detection is too dependent on the overflight dates from the sensors to make a comparison between the years meaningful. Furthermore, this post-flood assessment can be expanded by the statement that the higher the peaks are and the more stretched their distribution in the time dimension along the x-axis, the more hydrologically severe the flood event is. Consequently, the year 2007/2008 would be most affected, closely followed by 2008/2009 and 2016/2017 at least. Unfortunately, despite common peaks in the first two years of the study, no spatial similarities between the respective areas within these duration peaks could be identified. The reason for this should be due to fundamental differences in spatial origin and courses of the floods. The fact that although clear similarities in the 'Frequency Distribution' can be found is an evidence of a general drainage process or flooding course which can be spatially unbound. Further investigations are recommended, since a contribution to an integrated water resource management (IWRM) can be made by for example designating the most suitable and sustainable agricultural areas or for assigning high-risk areas to develop hazard managements within settlements.

6 Conclusion and Outlook

This study proves a suitable application of multi-sensor satellite data for the derivation of surface water products. By calculating the 'Maximum Water Extent', the 'Relative Frequency' and the 'Total Duration' for three flooded years in the Ilishana Zone, new insights into the complex hydrological system of the Ilishana Zone were gained. Especially a consideration not only of the

spatial extent, but also of the temporal dimension of the surface water allows new interpretations. Thus, three main statements could be made. First, each flood follows its own spatial concentration pattern, which confirms the strong dependence of the spatial distribution of precipitation. Secondly, the spatial extent of the connected drainage system, which drains into the Omadhiya Lakes, is strongly dependent on the amount of accumulated precipitation and the resulting interactivity of the *iishana*, due to the extremely shallow geomorphology and small-scale relief differences. Furthermore, the size of a connected network of clearly defined and regularly flooded channels is smaller than previously assumed. Thirdly, the inundation areas show a high temporal variability within the network, which illustrates the differences between pans and channels together with their respective hydrology.

The accuracy of the results of the last investigation year 2016/2017 shows the increasing potential of remote sensing data evaluation (Paganini et al. 2018; Wieland and Martinis 2019). By a recommended addition of optical Sentinel-2 data to the analysis, its radar twin-mission Sentinel-1 and the Landsat mission could in future allow freely available data in spatial resolution of less than 30m and a temporal coverage of at least one image per week. The increasing data density is also accompanied by a technological improvement in processing methods, whereby more reliable products could be created (Wieland and Martinis 2019). With a recommended annually gapless analysis of the Iishana Zone, including also the dry years, the seasonal variability and dynamic of surface water could be even better recorded on the basis of long-term series (Tulbure et al. 2016). The results of this study can and should also be used for further understanding of the hydrological system of the Iishana Zone: As example for derivation of water depths and water volume estimation, extraction of major drainage lines and connectivity between the *iishana*, for groundwater-refilling potential, absolute evapotranspiration estimations or for the improvement of hydrological models (Mason et al. 2016).

But above all there is potential in the application of these research findings, to generate usable and comprehensible products for local management. This is extremely important, since in times of more and intensified natural risks and a simultaneously rising demand on natural resources, the vulnerability to the lishana's population increases. (Angula and Kaundjua 2016; Calunga et al. 2015; Gilau et al. 2011; Newsham and Thomas 2011). Here 'Southern African Science Service Centre for Climate Change and Adaptive Land Management', a project for understanding climate and weather variabilities, also highlights the CB as one of five regional hotspots in South Africa (Helmschrot and Jürgens 2015; Kaspar et al. 2015).

A central network for flood management, especially within the rapidly growing cities like Oshakati and their illegal settlements (Muir and Hattingh 2012), should be implemented (Gilau et al. 2011). The SensorWeb project for northern Namibia (Frye et al. 2013; Kussul et al. 2012; Mandl et al. 2012) can be used as a starting point for fast response actions and can be supplemented by flood forecasting during events and hydrological models (Filali-Meknassi et al. 2014; Goormans et al. 2015; Hunukumbura et al. 2007; Mason et al. 2016; Mufeti et al. 2013).

Beside these natural, ecological factors there is a need of a transdisciplinary research, like social-ecological influences in resource management. IWRM strategies try to strengthen the ability of the system to adapt adequately to its land and water use by implementation of new technologies and creating a multi-resource mix (Kluge et al. 2008). Embedded in holistic and local IWRM projects, like CUVEwaters (Bischofberger et al. 2015; Ibisch et al. 2013; Klintenberg et al. October, 2007; Schulz et al. 2015), the states and local governance (Gilau et al. 2011; Ministry of Agriculture, Water and Forestry of Republic of Namibia 2011) as well as non-governmental organizations (Amadhila et al. 2013) can on site provide access to geographical information via maps or web services and moving forward together towards a sustainable and resilient future.

References

- Airbus Defence and Space. (2015). TerraSAR-X Image Product Guide: Basic and Enhance Radar Satellite Imagery. https://www.intelligence-airbusds.com/files/pmedia/public/r459_9_-20171004_tsxx-airbusds-ma-0009_tsx-productguide_i2.01.pdf. Accessed 10 December 2019.
- Amadhila, E., Shaamhula, L., van Rooy, G., & Siyambango, N. (2013). Disaster Risk Reduction in the Omusati and Oshana Regions of Namibia. *Jàmbá: Journal of Disaster Risk Studies*, 5(1).
- Angula, M. N., & Kaundjua, M. B. (2016). The changing Climate and Human Vulnerability in north-central Namibia. *Jamba (Potchefstroom, South Africa)*, 8(2), 200.
- Awadallah, A. G., & Tabet, D. (2015). Estimating Flooding Extent at high Return Period for ungauged braided Systems using Remote Sensing: A Case Study of Cuvelai Basin, Angola. *Natural Hazards*, 77(1), 255–272.
- Buckreuss, S., Werninghaus, R., & Pitz, W. (Eds.). (2008) *2008 IEEE Radar Conference, Rome, Italy, 26 - 30 May*.
- Calunga, P., Haludilu, T., Mendelsohn, J., Soares, N., & Weber, B. (2015). *Vulnerability in the Cuvelai Basin, Angola* (Occasional paper, no.12). Luanda, Angola: Development Workshop Angola.
- Christelis, G., & Struckmeier, W. (2001). *Groundwater in Namibia: An Explanation to the Hydrological Map* (1st ed.). Windhoek, Namibia: Department of Water Affairs.
- ESA. (2019a). ALOS PALSAR FBS, FBD and PLR products. <https://earth.esa.int/web/guest/-/alos-palsar-fbs-fbd-and-plr-products>. Accessed 5 January 2020.
- ESA. (2019b). User Guides - Sentinel-1 SAR - Sentinel Online. <https://sentinel.esa.int/web/sentinel/user-guides/sentinel-1-sar>. Accessed 5 December 2019.
- Farmer, G. T. (2015). *Modern Climate Change Science*. Cham: Springer International Publishing.

- Faulstich, L., Schulte, A., Arendt, R., Kavishe, F., & Lengricht, J. (2018). Quality of intensively used Surface Waters in the Cuvelai Basin (Northern Namibia) at the End of dry Season of 2017. *Geographica Augustana*(26).
- Frye, S., Percivall, G., Moe, K., Mandl, D., Handy, M., & Evans, J. (Eds.). (2013) *IEEE International Geoscience and Remote Sensing Symposium (IGARSS), Melbourne, Australia, 21 - 26 July 2013*. Piscataway, NJ: IEEE.
- Goormans, T., van Looveren, R., Mufeti, P., & Wynants, J. (Eds.). (2015) *E-proceedings of the 36th IAHR World Congress, Hageu, Netherlands, 28.06. - 03.07. .*
- Groeve, T. de. (2010). Flood Monitoring and Mapping using passive Microwave Remote Sensing in Namibia. *Geomatics, Natural Hazards and Risk*, 1(1), 19–35.
- Hassler, S. K., Kreyling, J., Beierkuhnlein, C., Eisold, J., Samimi, C., Wagenseil, H., et al. (2010). Vegetation pattern divergence between dry and wet season in a semiarid savanna – Spatio-temporal dynamics of plant diversity in northwest Namibia. *Journal of Arid Environments*, 74(11), 1516–1524.
- Helmschrot, J., & Jürgens, N. (2015). Integrated SASSCAL research to assess and secure current and future water resources in Southern Africa. *Proceedings of the International Association of Hydrological Sciences*, 366, 168–169.
- Hiyama, T., Suzuki, T., Hanamura, M., Mizuochi, H., Kambatuku, J. R., Niipele, J. N., et al. (2014). Evaluation of Surface Water Dynamics for Water-Food Security in seasonal Wetlands, north-central Namibia. *Proceedings of the International Association of Hydrological Sciences*, 364, 380–385.
- Hooli, L. J. (2016). Resilience of the poorest: Coping Strategies and indigenous Knowledge of Living with the Floods in Northern Namibia. *Regional Environmental Change*, 16(3), 695–707.

- Hunukumbura, P. B., Weerakoon, S. B., & Herath, S. (2007). Development of a cell-based Model to derive direct runoff Hydrographs for ungauged Mountainous Basins. *Journal of Mountain Science*, 4(4), 309–320.
- Ibisch, R., Kirschke, S., Stärz, C., & Borchardt, D. (2013). *Integriertes Wasserressourcenmanagement: Von der Forschung zur Umsetzung* (4th ed.). Leipzig, Germany.
- ICSMD. (2009). Flood in Northern Namibia: 27th of February 2009. <https://disasterscharter.org/web/guest/activations/-/article/flood-in-northern-namib-4>. Accessed 10 November 2019.
- Jensen, J. R. (2016). *Introductory digital image processing: A remote sensing perspective* (4th ed., Always learning). Glenview, Ill.: Pearson Education.
- Kaseke, K. F., Wang, L., Wanke, H., Turewicz, V., & Koeniger, P. (2016). An analysis of Precipitation Isotope Distributions across Namibia using historical Data. *PloS one*, 11(5), e0154598.
- Kaspar, F., Helmschrot, J., Mhanda, A., Butale, M., Clercq, W. de, Kanyanga, J. K., et al. (2015). The SASSCAL contribution to climate observation, climate data management and data rescue in Southern Africa. *Advances in Science and Research*, 12(1), 171–177.
- Kluge, T., Liehr, S., Lux, A., Moser, P., Niemann, S., Umlauf, N., et al. (2008). IWRM Concept for the Cuvelai Basin in northern Namibia. *Physics and Chemistry of the Earth, Parts A/B/C*, 33(1-2), 48–55.
- Kottek, M., Grieser, J., Beck, C., Rudolf, B., & Rubel, F. (2006). World Map of the Köppen-Geiger climate classification updated. *Meteorologische Zeitschrift*, 15(3), 259–263.
- Kussul, N., Mandl, D., Moe, K., Mund, J.-P., Post, J., Shelestov, A., et al. (2012). Interoperable infrastructure for Flood Monitoring: SensorWeb, Grid and Cloud. *IEEE Journal of Selected Topics in applied Earth Observations and Remote Sensing*, 5(6), 1–6.

- Leggett, K., Fennessy, J., & Schneider, S. (2003). Seasonal Vegetation Changes in the Hoanib River Catchment, north-western Namibia: A Study of a non-equilibrium System. *Journal of Arid Environments*, 53(1), 99–113.
- Li, J., & Yang, X. (Eds.). (2015). *Monitoring and Modeling of Global Changes: A Geomatics Perspective*. Dordrecht, Netherlands: Springer Netherlands.
- Long, S., Fatoyinbo, T. E., & Policelli, F. (2014). Flood Extent Mapping for Namibia using Change Detection and thresholding with SAR. *Environmental Research Letters*, 9(3), 35002.
- Lütke-meier, R., & Liehr, S. (2015). Impact of Drought on the Inhabitants of the Cuvelai Watershed: A qualitative Exploration. In J. Alvarez, A. Solera, J. Paredes-Arquiola, D. Haro-Monteagudo, & H. van Lanen (Eds.), *Drought: Research and Science-Policy Interfacing* (pp. 41–48): CRC Press.
- Mandl, D., Frye, S., Sohlberg, R., Cappelaere, P., Handy, M., & Grossman, R. (Eds.). (2012) *IEEE International Geoscience and Remote Sensing Symposium (IGARSS), Munich, Germany, 22 - 27 July*. Piscataway, NJ: IEEE.
- Marsh, A. (Ed.). (1992). *Oshanas: Sustaining people, environment and development in Central Owambo, Namibia*. s.l.: Typoprint.
- Martinis, S., Twele, A., & Voigt, S. (2009). Towards operational near real-Time Flood Detection using a split-based automatic Thresholding Procedure on high Resolution TerraSAR-X Data. *Natural Hazards and Earth System Sciences*, 9(2), 303–314.
- Martinis, S. (2010). *Automatic near real-Time Flood Detection in high Resoulution X-Band synthetic Aperture Radar Satellite Data using Context-based Classification on irregular Graphs*. Disstertation. Ludwig-Maximilians-Universität München, Munich, Germany.
- Martinis, S., Twele, A., & Voigt, S. (2011). Unsupervised Extraction of Flood-Induced Backscatter Changes in SAR Data Using Markov Image Modeling on Irregular Graphs. *IEEE Transactions on Geoscience and Remote Sensing*, 49(1), 251–263.

- Martinis, S., Twele, A., Strobl, C., Kersten, J., & Stein, E. (2013). A Multi-Scale Flood Monitoring System Based on Fully Automatic MODIS and TerraSAR-X Processing Chains. *Remote Sensing*, 5(11), 5598–5619.
- Martinis, S., Kersten, J., & Twele, A. (2015a). A fully automated TerraSAR-X based flood service. *ISPRS Journal of Photogrammetry and Remote Sensing*, 104, 203–212.
- Martinis, S., Kuenzer, C., Wendleder, A., Huth, J., Twele, A., Roth, A., et al. (2015b). Comparing four operational SAR-based Water and Flood Detection Approaches. *International Journal of Remote Sensing*, 36(13), 3519–3543.
- Martinis, S., Plank, S., & Ćwik, K. (2018). The Use of Sentinel-1 Time-Series Data to Improve Flood Monitoring in Arid Areas. *Remote Sensing*, 10(4), 583.
- Mason, D. C., Trigg, M., Garcia-Pintado, J., Cloke, H. L., Neal, J. C., & Bates, P. D. (2016). Improving the TanDEM-X Digital Elevation Model for Flood Modelling using Flood Extents from Synthetic Aperture Radar images. *Remote Sensing of Environment*, 173, 15–28.
- Mayr, M., & Samimi, C. (2015). Comparing the Dry Season In-Situ Leaf Area Index (LAI) Derived from High-Resolution RapidEye Imagery with MODIS LAI in a Namibian Savanna. *Remote Sensing*, 7(4), 4834–4857.
- Mendelsohn, J., & Weber, B. (2011). *Cuvelai: The Cuvelai Basin, its Water and People in Angola and Namibiaem Angola e Namibia* (Occasional paper, no. 8). Luanda, Angola: Development Workshop Angola.
- Mendelsohn, J., Jarvis, A., & Robertson, T. (2013). *A Profile and Atlas of the Cuvelai-Etosha Basin*. Windhoek, Namibia: RAISON; Gondwana Collection.
- Miranda, N. (2016). ASAR - Products Information. <https://earth.esa.int/web/sppa/mission-performance/esa-missions/envisat/asar/products-and-algorithms>. Accessed 13 December 2019.

- Mizuochi, H., Hiyama, T., Ohta, T., & Nasahara, K. (2014). Evaluation of the Surface Water Distribution in North-Central Namibia Based on MODIS and AMSR Series. *Remote Sensing*, 6(8), 7660–7682.
- Mufeti, P., Rientjes, T. H. M., Mabande, P., & Maathuis, B. H. P. (Eds.). (2013) *European Space Agency Living Planet Symposium, Edinburgh, UK, 9 - 13 September*.
- Newsham, A. J., & Thomas, D. S.G. (2011). Knowing, Farming and Climate Change Adaptation in North-Central Namibia. *Global Environmental Change*, 21(2), 761–770.
- Niipele, J. N., Kaholongo, I. K., & Njunge, J. (2015). Departure from indigenous Land Use System and the consequential Impacts: A Case of Cuvelai Basin, North-Central Namibia. *Journal of Environmental Science and Engineering A4*, 4(3).
- Oliver, C., & Quegan, S. (2004). *Understanding synthetic aperture radar images* (The SciTech radar und defense series). Raleigh, NC: SciTech Publishing Inc.
- Paganini, M., Petiteville, I., Ward, S., Dyke, G., Matthew, S., Harry, J., et al. (2018). *Satellite Earth Observations in Support of the Sustainable Development Goals: Special 2018 Edition*.
- Pekel, J.-F., Cottam, A., Gorelick, N., & Belward, A. S. (2016). High-resolution Mapping of Global Surface Water and its long-term Changes. *Nature*, 540(7633), 418–422.
- Persendt, F. C., Gomez, C., & Zavar-Reza, P. (2015). Identifying hydro-meteorological Events from Precipitation Extremes Indices and other Sources over northern Namibia, Cuvelai Basin. *Jamba (Potchefstroom, South Africa)*, 7(1), 177.
- Persendt, F. C. (2016). *Developing a Flood Hazard Analysis Framework in the Cuvelai Basin, Namibia, using a Flood Model, Remote Sensing, and GIS*. Doctorthesis. University of Canterbury, Christchurch, New Zealand.
- Persendt, F. C., & Gomez, C. (2016). Assessment of Drainage Network Extractions in a low-relief Area of the Cuvelai Basin (Namibia) from multiple Sources: LiDAR, Topographic Maps, and digital aerial Orthophotographs. *Geomorphology*, 260, 32–50.

- Potin, P., Rosich, B., Grimont, P., Miranda, N., Shurmer, I., O'Connell, A., et al. (Eds.). (2016) *Proceedings of EUSAR 2016: 11th European Conference on Synthetic Aperture Radar, Hamburg, Germany, 6 - 9 June*. Berlin, Offenbach: VDE Verlag.
- Rosenqvist, A., Shimada, M., Ito, N., & Watanabe, M. (2007). ALOS PALSAR: A Pathfinder Mission for Global-Scale Monitoring of the Environment. *IEEE Transactions on Geoscience and Remote Sensing*, 45(11), 3307–3316.
- Shakya, H. (2018). *Computing Flood Frequency and Duration from Earth Observation Data*. Masterthesis. Technical University of Munich, Munich, Germany.
- Shifidi, V. T. (2016). Impact of Flooding on rural Livelihoods of the Cuvelai Basin in Northern Namibia. *Journal of Geography and Regional Planning*, 9(6), 104–121.
- Skakun, S., Kussul, N., Shelestov, A., & Kussul, O. (2014). Flood Hazard and Flood Risk Assessment using a Time Series of Satellite Images: A Case Study in Namibia. *Risk analysis*, 34(8), 1521–1537.
- Strohbach, B. J. (2001). *Vegetation Survey of Namibia* (1st ed.). Windhoek, Namibia: Namibia Scientific Society.
- Strohbach, B. J. (2008). Mapping the major Catchments of Namibia. *Agricola*(18), 63–73.
- Thomson, M. (2018). Climate Change and Disaster Risk Management: Challenges and Opportunities. In S. L. Boulter (Ed.), *Natural disasters and adaptation to climate change* (Vol. 2, pp. 6–18). Cambridge: Cambridge Univ. Press.
- Töyrä, J., Pietroniro, A., & Martz, L. W. (2001). Multisensor Hydrologic Assessment of a Freshwater Wetland. *Remote Sensing of Environment*, 75(2), 162–173.
- Tulbure, M. G., Broich, M., Stehman, S. V., & Kommareddy, A. (2016). Surface Water Extent Dynamics from three Decades of seasonally continuous Landsat Time Series at subcontinental Scale in a semi-arid Region. *Remote Sensing of Environment*, 178, 142–157.

- Twele, A., Cao, W., Plank, S., & Martinis, S. (2016). Sentinel-1-based Flood Mapping: A fully automated Processing Chain. *International Journal of Remote Sensing*, 37(13), 2990–3004.
- United States Geological Survey. (2019). Landsat Satellite Missions. https://www.usgs.gov/land-resources/nli/landsat/landsat-satellite-missions?qt-science_support_page_related_con=2#qt-science_support_page_related_con. Accessed 4 January 2020.
- Wagenseil, H., & Samimi, C. (2007). Assessing spatio-temporal Variations in Plant Phenology using Fourier Analysis on NDVI time series: Results from a dry Savannah Environment in Namibia. *International Journal of Remote Sensing*, 27(16), 3455–3471.
- Wieland, M., & Martinis, S. (2019). A modular Processing Chain for automated Flood Monitoring from multi-spectral Satellite Data. *Remote Sensing*, 11(19), 2330.
- Williams, K. K., & Greeley, R. (2004). Laboratory and Field Measurements of the Modification of Radar Backscatter by Sand. *Remote Sensing of Environment*, 89(1), 29–40.
- ZKI. (2008). Überschwemmungen in Namibia: 17. März 2008. Deutsches Zentrum für Luft- und Raumfahrt. <https://activations.zki.dlr.de/de/activations/items/ACT047.html>. Accessed 11 November 2019.
- ZKI. (2009). Großräumiges Hochwasser im Norden Namibias: 01. März 2009. Deutsches Zentrum für Luft- und Raumfahrt. <https://activations.zki.dlr.de/de/activations/items/-ACT057.html>. Accessed 21 January 2020.

Declaration of Autonomy

'I hereby declare: I have composed this paper by myself and without any assistance other than the sources given in my list of works cited. This paper has not been submitted in the past or is currently being submitted to any other examination institution. It has not been published.'

A handwritten signature in black ink, appearing to read 'L. Berk', written in a cursive style.

Würzburg, 21th of February